AIAA JOURNAL
Vol. 42, No. 4, April 2004

Spatiotemporal Stability of Flow Through Collapsible, Viscoelastic Tubes

M. Hamadiche*
Ecole Centrale de Lyon, 69131 Ecully CEDEX, France
and
M. Gad-el-Hak†
Virginia Commonwealth University, Richmond, Virginia 23284

The stability of the Hagen–Poiseuille flow of a Newtonian fluid in an incompressible, collapsible, viscoelastic tube is determined using linear stability analysis. The dependence of the tube's diameter in the base state on the axial distance is explicitly accounted for in the present formulation. A novel numerical strategy is introduced to study the spatiotemporal stability of the coupled fluid-structure system subjected to infinitesimal axisymmetric or nonaxisymmetric disturbances. Axisymmetric disturbances correspond to the azimuthal wave number $n = 0$. There, we have identified two convective instability modes, one propagating upstream and the other downstream. For each of the nonaxisymmetric disturbances $n = 1$–6, we have found one absolute instability propagating upstream, whereas for $n = 1, 2$, downstream-propagating convective modes are additionally observed. Two of the standing waves have equal frequencies at their respective cusp points, while a third absolute instability has triple that frequency, in excellent agreement with existing experiments. The $n = 1$ absolute instability mode is replaced by a convective mode when the Reynolds number exceeds 200, while the other standing waves, at $n = 2$–6, persist to high Reynolds-number values. Increasing the solid's viscosity, thickness, or shear modulus causes the absolute instability modes to become convective as well as to ultimately become stable.

I. Introduction

FLUID conduits that are capable of collapse are commonly found in nature as well as in man-made systems. Although it might not be desirable for collapse to actually commence, numerous applications necessitate the use of soft tubing, in contrast to rigid pipes. Engine, fire and garden hoses, and many of the tubes used for medical and laboratory applications are made of elastic or viscoelastic materials and are designed so that collapse does not occur under normal operating conditions. In other applications, such as peristaltic pumps, blood transfusion, and assisted breathing, controlled collapsing is part of the design objective.

All fluid-carrying conduits in humans and other mammals are flexible and can collapse under sufficiently negative transmural pressure (internal pressure minus external pressure). Examples of tubes that can collapse as a result of trauma or disease are blood vessels, bronchial airways, and the gut. Conduits that do collapse during their normal operation include intramyocardial coronary blood vessels during systole, pulmonary blood vessels in the upper parts of the lung, large airways during forced expiration, urethra during micturition, and glottis during phonation.[1]

Internal pressure decreases along a constant-area duct conveying a viscous fluid, so that such a tube tends to collapse near the downstream end if the pressure external to the tube is sufficiently large. For prescribed external and inlet pressures and fluid and tube types, collapse will occur as the exit pressure is reduced in order to effect higher flow rates (i.e., higher Reynolds numbers). When collapsed, the cross section of a round tube becomes highly noncircular as shown in Fig. 1, and the flow rate is significantly reduced or even stopped, certainly the reverse of what is intended when the exit pressure is reduced. Two types of collapse are typically encountered, one in which the throat area asymptotes to a minimum and the resulting flow is steady, and the other where the throat area and axial position, flow rate, and exit conditions oscillate periodically or even chaotically despite constant supply conditions. Oscillating collapsible tubes are less common in vivo but are nevertheless observed when a vocal cord vibrates or when a brachial artery is compressed by a sphygmomanometer cuff, resulting in the so-called Korotkoff sound.

Because of their importance in medicine as well as technology and their intrinsic interest as complex dynamical systems, collapsible tubes have been extensively studied experimentally[2–11] as well as analytically and numerically.[12–24] The recent book by Carpenter and Pedley[25] contains two chapters that review the experimental and analytical aspects of collapsible tubes. The goal of these researches is to understand the phenomenon of collapse in order to prevent, control or exploit it.

A. Prior Experiments

In controlled experiments, a uniform flexible tube is typically mounted between two rigid pipes in a so-called Starling resistor configuration. The supply pressure is varied, and the pressure external to the compliant tube is controlled by surrounding the tube with a larger pressurized chamber. Observations are made of the collapse process (i.e., nonaxisymmetric buckling) and any accompanied oscillations in the throat area, the flow rate, and the exit pressure. Several noninvasive techniques have been developed to record the tube geometry during collapse, for example, X-ray cinefluorography,[26] stereophotogrammetric methods,[27] magnetic resonance imaging,[28] ultrasound imaging,[29] tomography,[30] and coded raster imaging.[7] Though invasive, conductimetric catheterization can be used to provide accurate time-dependent cross-sectional area of a collapsible tube during strictly repetitive oscillations.[8,31,32] In a totally different setting, the conductance catheter method is used widely to monitor in vivo the changing volume of heart chambers.[33]

Bertram and Godbole[9] used conductimetric catheterization to measure the instantaneous, shape-independent area at incrementally adjusted positions along the length of a collapsed, periodically

Received 15 April 2003; revision received 4 November 2003; accepted for publication 21 November 2003.

*Associate Professor, Laboratoire de Mécanique des Fluides et d'Acoustique.
†Caudill Eminent Professor and Chair, Department of Mechanical Engineering. Associate Fellow AIAA.

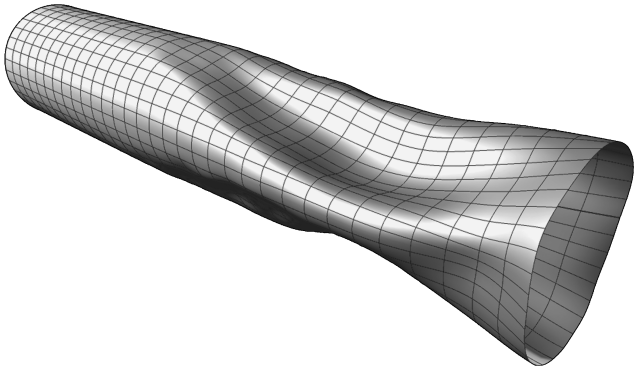

Fig. 1 Tube in a typical collapsed state.

oscillating tube. They observed three distinct modes of oscillations with sharp, discontinuous transitions separating them. Bertram and Godbole termed the two low-frequency modes *LU* and *LD* and the intermediate-frequency mode *I*. The low-frequency modes are distinguished by waveform shape: for *LU*, the collapse is brief relative to cycle length and is followed by a phase of relative quiescence; and for *LD*, the collapse lasts for approximately half the period. The third mode *I* has approximately three times the frequency of the other two and is obtained by transition from the brief-collapse mode as the appropriate parameter is varied. If the upstream pressure p_u is held constant, *LU* is the first mode observed as the downstream transmural pressure $p_{\mathrm{de}} = p_d - p_e$ is lowered to the point where collapse occurs and oscillations start, where p_d is the pressure at the downstream end of the tube and p_e is the pressure in the chamber surrounding the tube. Further reduction of p_{de} leads to either *LD* oscillations, at moderate p_u, or *I* oscillations at higher p_u.

B. Analytical Work

The full, unsteady, three-dimensional, fluid–solid interaction problem is intractable analytically or even numerically. As a result, simplified models have been attempted by several researchers. With few exceptions, these models fall in two categories: lumped-parameter models and one-dimensional models. In the former, the geometry of a collapsible segment is represented by one or two time-dependent variables such as the cross-sectional area at the narrowest point $A_N(t)$. The tube elastic properties are represented by a single-valued relationship between A_N and the transmural pressure at the narrowest point. The integral expressions for the conservation of mass, momentum, and energy result in a system of nonlinear ordinary differential equations whose solution can be steady or oscillatory. The lumped-parameter model is a global one but at the expense of giving a very crude description of local phenomena. Nevertheless the lumped-parameter model is capable of predicting small oscillations in the throat area and the flow rate despite constant supply conditions. Depending on the model parameters, these oscillations can be periodic or chaotic.

One-dimensional models, in which the flow is averaged over the tube's cross section, allow flow parameters such as tube area and velocity to vary in time and axial direction. A tube law relates the local transmural pressure to the local cross-sectional area. The resulting conservation laws are in the form of partial differential equations. The hyperbolic equations admit wave solutions, and the model predicts the breakdown of steady, one-dimensional flow when the cross-sectionally averaged fluid velocity exceeds the local value of the speed of propagation of small-amplitude pressure waves. Such supercritical conditions are analogous to choking of sonic gas flow in a nozzle: signals cannot be propagated upstream, and the flow rate and pressure gradient along the collapsible tube can vary independently of the upstream transmural pressure. The choking phenomenon is termed flow limitation in collapsible tubes literature, and can be associated with airway collapse and wheezing in humans when increasing a large expiratory driving pressure does not lead to an increase in flow rate.[23,34] The accompanied oscillations are generally much more pronounced than those predicted for subcritical flows.

The appearance of periodic or aperiodic oscillations has been attributed to more than one mechanism: choking in the one-dimensional models, or lack of steady solution or instability of the steady solution in the typically third- or fifth-order lumped-parameter models. Variation of viscous resistance with cross-sectional area and the unsteady head loss and pressure recovery in the jet forming in the diffuser region immediately downstream of the throat can all result in self-excited and self-sustained oscillations. Investigating the equilibrium states and their stability of a nonlinear, third-order lumped-parameter model, Bertram and Pedley[14] conclude that if there were no energy loss there would be no reopening and collapse would continue to zero area. If there were no pressure recovery, on the other hand, there would be no oscillations and all equilibria would be stable. Only if some energy loss and some pressure recovery are allowed are oscillations predicted by the model. Bertram and Pedley further conclude that pressure recovery is the only mechanism whereby the instability can derive energy from the flow.

The weakness of the lumped-parameter models is that they cannot incorporate wave propagation and therefore cannot distinguish between subcriticial and supercritical flows. One-dimensional models predict the onset of unsteady behavior at a particular point in the tube, but cannot be used to model the ensuing oscillations because they cannot incorporate either energy loss in the separated jet or the mechanical properties of the rigid tubes upstream and downstream of the elastic segment. For those reasons, Cancelli and Pedley[15] have proposed a composite model of a finite-length, collapsible tube, incorporating both one-dimensional, wave-propagation effects and the important aspects of the lumped-parameter models, including the inclusion of longitudinal wall tension in the description of the tube elastic properties and the modeling of energy loss in the separated jet in a way that is consistent with the one-dimensional flow equations.

In the limit of zero Reynolds number, Heil[20] has computed the steady deformations of a fully coupled three-dimensional system consisting of a Stokes flow in a nonaxisymmetric cylindrical shell simulating a collapsed round tube. Recently, Luo and Pedley[23] have conducted numerical simulations of the steady and unsteady flows in a two-dimensional channel where a portion of its upper wall is replaced by a collapsible, tensioned membrane. Luo and Pedley found multiple steady solutions for a range of upstream transmural pressures and Reynolds numbers. Stability analysis of these steady solutions indicates that there is no one-to-one correlation between flow limitation and self-excited oscillations, at least in their particular two-dimensional model. Finally, Pedley[24] provides a succinct review of linear and nonlinear analysis of blood flow in collapsible arteries and veins in vertebrates and other large animals.

C. Present Work

In the present research, we take the view that collapse and oscillations can be the climactic manifestation of an instability of the coupled fluid–tube system. Therefore, we study the linear stability of the system prior to the onset of time-dependent collapse. This approach clearly excludes the complex flow associated with the geometry of a noncircular, convergent–divergent nozzle and the oscillations caused by the choking phenomenon, but allows us to investigate a first-principles, arbitrary-Reynolds-number system that is much more general and less ad hoc than that afforded by the lumped-parameter, the one-two-dimensional or the zero-Reynolds-number models.

We start with a distended, constant-diameter tube made of viscoelastic material, as shown schematically in Fig. 2. The Navier–Stokes equations describe the fluid side, and the Navier equation describes the compliant tube side. As a base state, we assume a finite-length flexible tube anchored at both ends and surrounded by a large pressurized chamber of constant pressure. As a result of a pressure-driven base flow inside, the tube is subjected, along its length, to an increasingly negative transmural pressure. Consequently, the flexible tube deforms slightly into a convergent–divergent geometry (or a

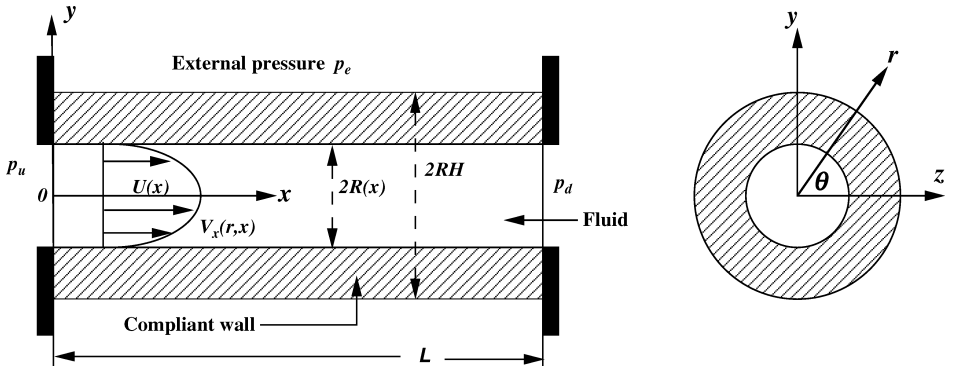

Fig. 2 Coordinate system and tube geometry.

divergent–convergent one in case of a positive transmural pressure). For sufficiently stiff tubes, the base geometry is axisymmetric, and the tube diameter is a weak function of the axial coordinate. We explicitly compute this function using the steady equation of linear elasticity. However, the base flow inside the convergent–divergent channel is assumed, to first order, to be locally parallel and parabolic.

The locally parallel Hagen–Poiseuille flow, the pressure gradient inside, the external pressure, and the tube's geometry, thickness, and viscoelastic properties are all specified as a base state of the coupled dynamical system. It is assumed that for each specified set of parameters, all of the forces resulting from the steady flow, the tube stiffness, and the external pressure are initially in static equilibrium (but not necessarily stable equilibrium) to yield a motionless, convergent–divergent tube capable of dynamically deforming when perturbed. We subject the coupled fluid-tube system to axisymmetric as well as nonaxisymmetric perturbations and study the spatiotemporal instability of that dynamical system. The linearized Navier–Stokes and Navier equations are coupled via proper boundary conditions at the fluid–solid interface and describe the early stages of the imposed perturbation dynamics. Both inertial and viscous forces are retained in the formulation, allowing for an arbitrary Reynolds number.

The present work is a natural extension of our previous study of the stability of noncollapsible, soft tubes[35] (see also Evrensel et al.,[36] Kumaran,[37] and the many references in all three papers). There, a rigid shell surrounds the compliant tube, thus preventing collapse while admitting other types of tube deformation. The primary difference in formulation of the original study and the present one is therefore in the boundary condition at the outer surface of the viscoelastic tube: motionless compliant-rigid interface in the former study and no stresses at the free surface in the new study. A second difference is that we study in here the spatiotemporal instability of the system, whereas in the original paper we considered only the temporal instability. The present extension will allow us to make precise determination of whether a particular instability is absolute or convective. The parameters of the present system are chosen such that it is stable if the compliant duct is not allowed to collapse (à la our previous study[35]). In this way, any unstable mode found is expected to be unique to collapsible tubes. We utilize the same numerical method introduced in Hamadiche and Gad-el-Hak[35] to study, without a need for an initial guess, the stability of the coupled fluid–structure system.

The present paper is organized as follows. Following these introductory remarks, the base state, the linearized equations of motion, and the numerical approach are described in Sec. II. This is followed in Sec. III by the computed results of the stability of the system to axisymmetric and nonaxisymmetric disturbances. Finally, concluding remarks are given in Sec. IV.

II. Problem Formulation and Numerical Approach

We wish to study the stability of an incompressible, Newtonian fluid of density ρ, viscosity μ, and maximum axial velocity $U(x)$, flowing in a compliant tube of inner radius $R(x)$, which weakly depends on the axial distance and outer radius RH, where $(H-1)$ is a prescribed thickness parameter. The finite tube is anchored at both ends and has a length L. The compliant wall is made of an incompressible, viscoelastic material of density ρ equal to the fluid density, viscosity μ_s, and shear modulus G. The surface $r = RH$ of the pliable material is a free surface and is, accordingly, free to move. In the remainder of this paper, dimensionless variables will be used unless otherwise indicated. The length scale is the radius of the tube at its entrance $R(0)$, the timescale is $[\rho R^2(0)/G]^{1/2}$, and the velocity scale is $V_{\text{ref}} = (G/\rho)^{1/2}$. Pressure is nondimensionalized as follows: $p|_{\text{dimensionless}} = (p - p_u)/G$, where p_u is the upstream (inlet) pressure. Except for the boundary condition at the outer surface of the compliant tube and the fact that we account for the variable tube diameter in the base state, the governing equations are similar to those developed in Hamadiche and Gad-el-Hak[35] for the case of a compliant tube contained within a rigid shell. For completeness, however, the entire system of equations is briefly recalled herein.

A. Wall Curvature

Under the first-order assumption that the flow is locally parallel, the pressure in the duct falls downstream as

$$p(x) = -4\Gamma Re^{-1}x \tag{1}$$

where $\Gamma = [\rho U^2(x)/G]^{1/2}$, and the local Reynolds number is $Re = \rho V_{\text{ref}} R(x)/\mu$. (Though the tube's length is finite, the system stability is studied under the assumption of locally parallel flow, which is tantamount to assuming an infinitely long tube. Relaxing that assumption makes the analysis considerably more involved.) The dimensionless variable Γ is a local measure of the relative compliance of the coating because an increase in its value implies a relatively softer material. For the case where the external pressure p_e is equal to the inlet pressure p_u, the viscous losses in the fluid lead to an increasingly more negative transmural pressure $[p(x) - p_e]$ as x increases.

To find the form of the duct under the influence of the transmural pressure, we solve the steady, linear elasticity equation

$$\partial_j^2 u_i = \partial_i p \tag{2}$$

where u_i and p are, respectively, the wall displacement and pressure. We seek a solution in the cylindrical coordinates (r, θ, x) where the components of the displacement vector are (u_r, u_θ, u_x). To first order, the azimuthal and axial displacements are null, and the radial displacement depends only on x. Thus $[u_r(x), 0, 0]$, which identically satisfies the continuity equation. Substituting this particular solution in the linear elasticity equation leads to

$$\mathrm{d}_x^2 u_r = \mathrm{d}_r p \tag{3}$$

where d_x and d_r stand for derivative with respect to axial and radial coordinates, respectively. Because the left-hand side of Eq. (3) is a function of x only, the right-hand side must be independent of r. Thus, the radial derivative of the pressure inside the solid depends on x only. In other words, the pressure derivative with respect to r is constant across the thickness of the tube and is equal to the

negative of the transmural pressure divided by the thickness of the wall. Thus,

$$\mathrm{d}_r p = \frac{\left(p_e + 4\Gamma Re^{-1}x\right)}{(H-1)} \tag{4}$$

the radial displacement Eq. (3) becomes

$$\mathrm{d}_x^2 u_r = \frac{\left(p_e + 4\Gamma Re^{-1}x\right)}{(H-1)} \tag{5}$$

The tube is anchored at both ends, and therefore the boundary conditions are

$$u_r|_{x=0} = u_r|_{x=L} = 0 \tag{6}$$

The solution of Eq. (5) with boundary conditions (6) is

$$u_r = \frac{p_e}{2(H-1)}(x^2 - Lx) + \frac{4\Gamma}{6Re(H-1)}(x^3 - L^2 x) \tag{7}$$

For modest transmural pressures and sufficiently stiff tubes, u_r is small. It is negative for negative transmural pressure (tube collapses) and positive when the fluid pressure exceeds that of the external chamber (tube blows up). The preceding radial wall displacement is related to the dimensionless tube radius, thus,

$$\delta(x) \equiv R(x)/R(0) = 1 + u_r(x) \tag{8}$$

Therefore, for a negative transmural pressure the radius of the tube in the base state gently decreases downstream, reaching a minimum at a position that depends on the Reynolds number, tube stiffness, and relative strength of the external pressure, then increases back to the inlet radius $R(0)$. The first-order theory developed herein assumes $\delta'/\delta \ll 1$, where the prime denotes derivative with respect to x.

B. Mean Flow

Although the tube radius is a function of axial distance, the base flow is, to first order, locally parallel. The base flow velocity components are

$$[V_r, V_\theta, V_x] = [V_r(r,x), 0, V_x(r,x)] \tag{9}$$

where

$$V_x(r,x) = \Gamma(x)(1 - r^2/\delta^2) \tag{10}$$

Note that the variable Γ is related to the (dimensional) volume flux Q_v and the (dimensional) velocity on the axis of the tube $U(x)$ by the equation

$$\Gamma = \frac{U(x)}{V_{\mathrm{ref}}} = \frac{2Q_v}{\pi R^2(x) V_{\mathrm{ref}}} \tag{11}$$

We use the continuity equation to compute the base radial velocity component. In cylindrical coordinates and for axisymmetric base flow,

$$(1/r)\partial_r(rV_r) = -\partial_x V_x \tag{12}$$

The solution is

$$V_r(r,x) = \delta'\Gamma(x)(r/\delta - r^3/\delta^3) \tag{13}$$

where the prime denotes derivative with respect to x. Clearly, $V_r \ll V_x$ for gently changing tube diameter, and the assumption of a locally parallel flow is justified.

Introducing the similarity variables

$$X = x, \qquad \eta = r/\delta \tag{14}$$

the base flow axial and radial velocity components are then

$$V_x = \Gamma(X)(1-\eta^2), \qquad V_r = \delta'\Gamma(X)(\eta - \eta^3) \tag{15}$$

In the perturbation equations developed in the following section, partial derivatives with respect to r and x are given in terms of the similarity variables as follows:

$$\partial_r = (1/\delta)\partial_\eta, \qquad \partial_x = \partial_X - (\delta'\eta/\delta)\partial_\eta \tag{16}$$

C. Disturbance Equations

The governing equations for the fluid are the Navier–Stokes mass and momentum equations

$$\partial_i v_i = 0 \tag{17}$$

$$\partial_t v_i + v_j \partial_j v_i = -\partial_i p + \epsilon\Gamma\partial_j^2 v_i \tag{18}$$

where $\partial_t = \partial/\partial t$, $\partial_j = \partial/\partial x_j$, and $\epsilon = Re^{-1}$. For a Hagen–Poiseuille flow, specifying the Reynolds number for a given fluid and tube radius and length is tantamount to specifying the maximum velocity, flow rate, and mean pressure gradient. The instantaneous fluid pressure p is offset by the inlet pressure p_u and nondimensionalized by the shear modulus G.

The compliant wall of the tube is modeled using the dynamical equations for an incompressible, viscoelastic material.[38] The dynamics of the wall is described by a displacement field u_i, which represents the displacement of material points from their steady-state positions as a result of the fluid stresses perturbing the interface. For an incompressible material, the displacement field u_i satisfies the solenoidal condition

$$\partial_i u_i = 0 \tag{19}$$

and the momentum conservation equation is

$$\partial_t^2 u_i = -\partial_i p + \partial_j^2 u_i + \epsilon\Gamma\mu_r\partial_j^2 v_i \tag{20}$$

The left-hand side represents the rate of change of momentum in a volume element, while the three terms on the right-hand side are, respectively, the divergence of the pressure, the divergence of the elastic stress caused by the strain in the material, and the divergence of the viscous stress caused by the strain rate. In the latter term, the wall velocity is given by $v_i = \partial_t u_i$, and $\mu_r = \mu_s/\mu$. The relative viscosity μ_r is zero for elastic solids.

D. Nonaxisymmetric Disturbances

In linear stability analysis, small perturbations in the form of Fourier modes are introduced in the fluid velocity field and the wall displacement field:

$$(v_j, p) = (\tilde{v}_j, \tilde{p})\exp(ikX + in\theta + st) + cc \tag{21}$$

$$(u_j, p) = (\tilde{u}_j, \tilde{p})\exp(ikX + in\theta + st) + cc \tag{22}$$

where $\tilde{v}_j$ and $\tilde{u}_j$ are the eigenfunctions that are functions of η only, the real part of the complex k is the axial wave number, the negative of its imaginary part is the spatial growth rate of the perturbation (for positive X), n is the azimuthal wave number that is taken as real in the present formulation, p is the pressure disturbance, and cc stands for complex conjugate. The real part of the eigenvalue s is the temporal growth rate of the perturbation, and the imaginary part is the radian frequency. Upon inserting the preceding perturbation velocity (21) into the conservation equations for the fluid velocity field (17) and (18) and neglecting the nonlinear terms in $\tilde{v}_j$, the following linear, ordinary differential equations are obtained for the eigenfunction $\tilde{v}_j$ in cylindrical coordinates:

$$\left[\mathrm{d}_\eta + \eta^{-1}\right]\tilde{v}_r + ik\delta\tilde{v}_x + in\eta^{-1}\tilde{v}_\theta - \delta'\eta\,\mathrm{d}_\eta\tilde{v}_x = 0 \tag{23}$$

$$\begin{aligned}[s + \Gamma ik(1-\eta^2)]\tilde{v}_r + h\delta^{-1}\mathrm{d}_\eta\tilde{v}_r + \delta^{-1}\tilde{v}_r\partial_\eta V_r &= -\delta^{-1}\mathrm{d}_\eta\tilde{p} \\ &+ \delta^{-2}\epsilon\Gamma\left\{\left[\mathrm{d}_\eta^2 + \eta^{-1}\mathrm{d}_\eta + 2ik\delta\,\mathrm{d}_\eta - \eta^{-2}(1+n^2) - \delta^2k^2\right]\tilde{v}_r\right. \\ &\left. - 2in\eta^{-2}\tilde{v}_\theta\right\}\end{aligned} \tag{24}$$

$$[s+\Gamma ik(1-\eta^2)]\tilde{v}_x + h\delta^{-1}\,\mathrm{d}_\eta \tilde{v}_x - 2\Gamma\delta\eta\tilde{v}_r$$
$$= -ik\tilde{p} + \delta^{-1}\delta'\eta\,\mathrm{d}_\eta\tilde{p} - \tilde{v}_x\partial_X V_x - \delta^{-1}\tilde{v}_r\partial_\eta V_x$$
$$+\delta^{-2}\epsilon\Gamma\left[\mathrm{d}_\eta^2 + \eta^{-1}\,\mathrm{d}_\eta + 2ik\delta\,\mathrm{d}_\eta - (\delta^2k^2 + n^2\eta^{-2})\right]\tilde{v}_x \quad (25)$$

$$[s+\Gamma ik(1-\eta^2)]\tilde{v}_\theta + h\delta^{-1}\,\mathrm{d}_\eta\tilde{v}_\theta = in(\delta\eta)^{-1}\tilde{p}$$
$$+\delta^{-2}\epsilon\Gamma\left\{\left[\mathrm{d}_\eta^2 + \eta^{-1}\,\mathrm{d}_\eta + 2ik\delta\,\mathrm{d}_\eta - \eta^{-2}(1+n^2) - \delta^2k^2\right]\tilde{v}_\theta\right.$$
$$\left.+\,2in\eta^{-2}\tilde{v}_r\right\} \quad (26)$$

where d_η stands for derivative with respect to η, $h = V_r - \delta'\eta$, and $\tilde{p}(\eta)$ is the eigenfunction for the pressure.

Similarly, the equations for the eigenfunction $\tilde{u}_j$ can be obtained by inserting the equation for the solid displacement perturbation (22) into the conservation equations (19) and (20), yielding in cylindrical coordinates

$$[\mathrm{d}_\eta + \eta^{-1}]\tilde{u}_r + ik\delta\tilde{u}_x + in\eta^{-1}\tilde{u}_\theta - \delta'\eta\,\mathrm{d}_\eta\tilde{u}_x = 0 \quad (27)$$

$$s^2\tilde{u}_r = -\delta^{-1}\,\mathrm{d}_\eta\tilde{p} + \delta^{-2}(1+\epsilon\Gamma\mu_r s)\left\{\left[\mathrm{d}_\eta^2 + \eta^{-1}\,\mathrm{d}_\eta\right.\right.$$
$$\left.\left.+\,2ik\delta\,\mathrm{d}_\eta - \eta^{-2}(1+n^2) - \delta^2k^2\right]\tilde{u}_r - 2in\eta^{-2}\tilde{u}_\theta\right\} \quad (28)$$

$$s^2\tilde{u}_x = -ik\tilde{p} + \delta^{-1}\delta'\eta\,\mathrm{d}_\eta\tilde{p} + \delta^{-2}(1+\epsilon\Gamma\mu_r s)\left[\mathrm{d}_\eta^2 + \eta^{-1}\,\mathrm{d}_\eta\right.$$
$$\left.+\,2ik\delta\,\mathrm{d}_\eta - (\delta^2k^2 + n^2\eta^{-2})\right]\tilde{u}_x \quad (29)$$

$$s^2\tilde{u}_\theta = -in\delta^{-1}\eta^{-1}\tilde{p} + \delta^{-2}(1+\epsilon\Gamma\mu_r s)\left\{\left[\mathrm{d}_\eta^2 + \eta^{-1}\,\mathrm{d}_\eta\right.\right.$$
$$\left.\left.+\,2ik\delta\,\mathrm{d}_\eta - \eta^{-2}(1+n^2) - \delta^{-2}k^2\right]\tilde{u}_\theta + 2in\eta^{-2}\tilde{u}_r\right\} \quad (30)$$

The boundary conditions at the center of the tube $\eta = 0$, applied to the azimuthally varying modes with azimuthal wave number $n = 1$, are

$$\tilde{v}_r + i\tilde{v}_\theta = 0 \quad (31)$$

$$\tilde{v}_x = \tilde{p} = 0 \quad (32)$$

at the interface $\eta = 1$:

$$\tilde{v}_r = s\tilde{u}_r \quad (33)$$

$$\tilde{v}_x - 2\Gamma\tilde{u}_r = s\tilde{u}_x \quad (34)$$

$$\tilde{v}_\theta = s\tilde{u}_\theta \quad (35)$$

$$-\tilde{p}_s + \tilde{\sigma}_{rr} + \delta'\tilde{\sigma}_{rx} = -\tilde{p}_f + \tilde{\tau}_{rr} + \delta'\tilde{\tau}_{rx} \quad (36)$$

$$\tilde{\sigma}_{r\theta} + \delta'\tilde{\sigma}_{x\theta} = \tilde{\tau}_{r\theta} + \delta'\tilde{\tau}_{x\theta} \quad (37)$$

$$\tilde{\sigma}_{rx} + \delta'(-\tilde{p}_s + \tilde{\sigma}_{xx}) = \tilde{\tau}_{rx} + \delta'(-\tilde{p}_f + \tilde{\tau}_{xx}) \quad (38)$$

The term $-2\Gamma\tilde{u}_r$ in Eq. (34) represents the variation of the mean velocity at the interface as a result of the surface displacement. The subscripts s and f refer to the solid and fluid medium, respectively, and σ and τ are the components of the stress tensor in the solid and in the fluid, respectively. The terms multiplied by δ' appear because of the wall curvature, as will be explained next.

To find the boundary condition at the free surface, let $[r - \delta = \text{constant}]$ be the equation of the free surface. The normal $\boldsymbol{n}$ to the surface is in the direction of the gradient of the function $r - \delta$, namely,

$$\boldsymbol{n} = \frac{\nabla(r-\delta)}{|\nabla(r-\delta)|} = \frac{(1,0,\delta')}{(1+\delta'^2)^{0.5}} \cong (1,0,\delta') \quad (39)$$

As there is no traction at the free surface, the boundary condition at the free surface becomes

$$-p\boldsymbol{n} + \bar{\bar{\sigma}}\cdot\boldsymbol{n} = 0 \quad (40)$$

this leads to the following equations:

$$-\tilde{p} + \tilde{\sigma}_{rr} + \delta'\tilde{\sigma}_{rx} = 0 \quad (41)$$

$$\tilde{\sigma}_{r\theta} + \delta'\tilde{\sigma}_{x\theta} = 0 \quad (42)$$

$$\tilde{\sigma}_{rx} + \delta'(-\tilde{p} + \tilde{\sigma}_{xx}) = 0 \quad (43)$$

The boundary conditions at $\eta = 0$, applied to the two components of nonaxisymmetric eigenmodes $(\tilde{v}_r, \tilde{v}_\theta)$ with azimuthal wavenumber $n > 1$, are

$$\tilde{v}_r = \tilde{v}_\theta = 0 \quad (44)$$

The remaining boundary conditions are identical to those applied to the eigenmodes with azimuthal wave number $n = 1$.

The linearized mass and momentum equations for the fluid and solid can be transformed to a system of first-order differential equations. The procedure is straightforward, and the resulting system of 12 first-order, linear, ordinary differential equations is similar to that in our previous paper.[35]

To study the spatiotemporal stability of the coupled system to axisymmetric disturbances, small perturbations in the form of axisymmetric Fourier modes are introduced in the fluid velocity field and the wall displacement field. The linear system of equations related to axisymmetric disturbances can readily be obtained by inserting $n = 0$, $\tilde{v}_\theta = 0$, and $\tilde{u}_\theta = 0$ into the system of differential equations and boundary conditions just developed for the nonaxisymmetric disturbances.

E. Spatiotemporal Instability

Hydrodynamic instabilities can be classified as convective or absolute based on the linear response of the system to an initial localized impulse.[39–45] This notion and its theoretical underpinning were first developed and applied to the study of plasma instabilities.[46,47] A flow is convectively unstable if, at any fixed location, this response eventually decays in time—in other words, if all growing disturbances convect downstream from their source. Convective instabilities occur when there is no mechanism for upstream disturbance propagation, as for example in the case of rigid-wall, nonseparating boundary layers. If the disturbance is removed, then perturbation propagates downstream, and the flow relaxes to an undisturbed state. Suppression of convective instabilities is particularly effective when applied near the point where the perturbations originate.

If the flow is absolutely unstable, there is at least one growing mode having zero group velocity. This means that the local system response to an initial impulse grows in time. Absolute instabilities can occur when a mechanism exists for upstream disturbance propagation, as for example in the separated flow over a backward-facing step where the flow recirculation provides such mechanism. In this case, some of the growing disturbances can travel back upstream and continually disrupt the flow even after the initial disturbance is neutralized. Flow oscillations in this case are self-excited. Therefore, absolute instabilities are generally more dangerous and more difficult to control; nothing short of complete suppression will work. In some flows, for example, two-dimensional blunt-body wakes, certain regions are absolutely unstable while others are convectively unstable. The upstream addition of acoustic or electric feedback can change a convectively unstable flow to an absolutely unstable one and self-excited flow oscillations can thus be generated. In any case, identifying the character of flow instability facilitates its effective control (i.e., suppressing or amplifying the perturbation as needed).

Huerre[44] provides a concise description of how to determine whether a particular instability is absolute or convective. The paper by Doaré and de Langre[48] best describes the concept of local and global instabilities in the context of a fluid–structure interaction problem. In this section, we provide only the theory highlights. For a linear system, the impulse response is given by the Green function that can be solved in the (k, ω) space and is expressed as the double Fourier integral

$$G(x,t) = \frac{1}{(2\pi)^2}\int_{F_k}\int_{L_\omega}\frac{\exp[i(kx-\omega t)]}{D[k,\omega;Re]}\,\mathrm{d}\omega\,\mathrm{d}k \quad (45)$$

where D is the dispersion relation, and k and ω are, respectively, the complex wave number and complex frequency. The path F in the complex wave-number plane is initially taken along the real axis. The contour L in the complex frequency plane is a straight

horizontal line located above all of the singularities of the integrand so as to satisfy causality, that is, effect cannot precede cause.

In most cases, the Fourier–Laplace integration in Eq. (45) cannot be evaluated readily for all t. It is sufficient, however, to compute the long-term behavior of $G(x,t)$ along different spatiotemporal rays $x/t = \text{constant}$. The time-asymptotic (large t, fixed x/t) Green function is readily computed by the well-known method of analytic continuation in which the Laplace contour L is deformed toward the lower half of the complex ω plane, yielding

$$G(x,t) = -\frac{i}{2\pi}\int_{F_k} \frac{\exp\{i[kx - \omega(k)t]\}}{(\partial D/\partial\omega)[k, w(k); Re]}\,\mathrm{d}k \qquad (46)$$

An instability mode is considered to be absolute if there is a "pinch point" in the Fourier contours that prevents the temporal amplification rate from being reduced down to zero. If there are no pinch points, the instability mode is convective. In other words, observing a pinch point in the unstable zone of the Fourier plane is a necessary and sufficient condition for the presence of an absolute instability.

In the case of an absolute instability, the mode propagates upstream as well as downstream and often has a very small (or even zero) group velocity in comparison with the velocity of the mean flow. The coalescence of two modes coming from different halves of the wave-number plane can be detected by inspection of the dispersion relation. The existence of a pinch point is equivalent to the existence of a saddle point of the dispersion relation in the complex wave-number plane formed by two modes coming from two different halves of that plane. Kupfer et al.[47] have shown that such a saddle point is equivalent to a cusp point in the complex frequency plane, that is, in the Laplace contours. Kupfer et al. provide fuller account of the procedure outlined here.

F. Numerical Method

The system of six first-order differential equations describing the evolution of the nonaxisymmetric fluid disturbances and their equivalents for the axisymmetric fluid disturbances were solved using a fourth-order Runge–Kutta method to arrive at three independent solutions $(\boldsymbol{X}_1, \boldsymbol{X}_2, \boldsymbol{X}_3)$, each of which satisfy the boundary conditions at $\eta = 0$. The independence of the three solutions is ensured by starting the computation with one of the three independent vectors formed by several values of the vector $(\xi_r, \xi_\theta, \xi_x)$ at $\eta = 0$, where $(\xi_r, \xi_\theta, \xi_x)$ are the derivatives of (v_r, v_θ, v_x) with respect to η. The chosen values must form a free set of vectors. During the computation, the vectors are orthonormalized at each step in order to preserve their linear independence and thus achieve rapid convergence.[49]

Similarly, for the displacement field in the solid we obtain three independent solutions $(\boldsymbol{Y}_1, \boldsymbol{Y}_2, \boldsymbol{Y}_3)$, each of which satisfy the boundary conditions at $\eta = H$. The independence of the solutions is ensured as well by beginning the computation with one of the three independent vectors formed by several values of the vector $(\chi_r, \chi_\theta, \chi_x)$ at $\eta = H$, where $(\chi_r, \chi_\theta, \chi_x)$ are the derivatives of (u_r, u_θ, u_x) with respect to η.

The boundary conditions at $\eta = 1$ lead to the eigenvalue problem $\boldsymbol{MC} = 0$, where the elements of the 6×6 matrix $\boldsymbol{M}$ are a linear combination of the particular solution components $(\boldsymbol{X}_1, \boldsymbol{X}_2, \boldsymbol{X}_3)$, $(\boldsymbol{Y}_1, \boldsymbol{Y}_2, \boldsymbol{Y}_3)$ and their derivatives with respect to η at $\eta = 1$, which involve k, n, p_e, Re, Γ, H, and μ_r. The components of the vector $\boldsymbol{C}$ are the six arbitrary constants appearing in the general solutions in the fluid and solid media.

The characteristic equation is obtained by setting the determinant of $\boldsymbol{M}$ to zero. To use the continuation method, the derivative with respect to s of this determinant is computed, where s is the complex eigenvalue of the coupled system. For this, the derivative with respect to s of the linearized mass and momentum equations is needed, which leads to another system of first-order differential equations.

The resulting system is solved using a fourth-order Runge–Kutta scheme. This leads to the derivative with respect to s of the elements of the matrix $\boldsymbol{M}$, which gives the derivative of the determinant of $\boldsymbol{M}$. The solution of the characteristic equation gives the growth rate as function of the Reynolds number for different values of the parameters k, n, p_e, Γ, H, and μ_r. The effects of changes in the parameter values on the system stability are examined in Sec. III for both the axisymmetric and nonaxisymmetric disturbances.

G. Eigenvalue Search Technique

The application of the boundary conditions at the fluid–solid interface leads to the following eigenvalue problem:

$$\boldsymbol{MC} = 0 \qquad (47)$$

where the elements of the 6×6 matrix $\boldsymbol{M}$ depend on the components of the particular solutions. The method proposed by Garg and Rouleau[50] to compute the number of poles of a complex function lying within a closed curve was extended by Hamadiche[51,52] to determine all of the singularities of a complex function lying within a closed region in the complex eigenvalue plane. This method, which was limited at each step to three modes and needed a recurrence formula to compute more than three modes, is extended herein to an arbitrary number of modes at each step as follows. Let $f(z)$ be the determinant of the matrix $\boldsymbol{M}$. This function is assumed a priori and later verified to be analytic. Cauchy's theorem gives

$$2\pi(N - P) = \int_C f(z)^{-1}\frac{\partial f(z)}{\partial z}\,\mathrm{d}z \qquad (48)$$

where N and P denote, respectively, the number of zeros and the number of poles of the function $f(z)$, counted with their multiplicity, within the closed region C. Because the determinant is an analytic function of the complex eigenvalue s, we have

$$\int_C f(z)\,\mathrm{d}z = 0 \qquad (49)$$

so that $P = 0$. In our computation, the curve C is a circle centered on the origin of the complex z plane. Knowing the number of zeros of the determinant N, which is the number of eigenmodes, we can use Cauchy's theorem and the theorem of residues to evaluate the sum of eigenvalues as well as the sum of their jth power inside the closed region C. Thus,

$$2i\pi\sum_{m=1}^{m=N} z_m^j = \int_C z^j f(z)^{-1}\frac{\partial f(z)}{\partial z}\,\mathrm{d}z = 2i\pi Q_j \qquad (50)$$

During the summation, the exponent j is held constant, and z_m is the value of the complex variable z in the pole m, which is the desired eigenvalue. Having the number of zeros N from Eq. (48), the system (50) contains N nonlinear equations, which in principle allows us to determine the eigenvalues. The system (50) has a Vandermonde matrix structure. Therefore, the eigenmodes z_m are the root of the following polynomial[53]:

$$\boldsymbol{P}(z) = z^n - \sigma_1 z^{n-1} + \cdots + (-1)^k\sigma_k z^{n-k} + \cdots + (-1)^n\sigma_n \qquad (51)$$

where σ_k are given by the following recurrence formula:

$$k(-1)^k\sigma_k = -(Q_k - \sigma_1 Q_{k-1} + \cdots + \sigma_{k-1}Q_1) \qquad (52)$$

As has been shown by Lelong-Ferrand and Arnaudiès,[53] the roots of the polynomial $\boldsymbol{P}$ are the required solution that can be obtained by traditional computer library routines. The present novel methodology eliminates the constraint imposed on the number of modes inside the closed region in the complex eigenvalue plane. For very large N, where traditional procedures to compute the polynomial roots might not readily converge, one can revert to the iterative technique proposed and used by Hamadiche[52] in order to lower the degree of the polynomial. Procedures available in the usual computer libraries readily converge for polynomial degree much higher than three. The continuation method permits the computation of the eigenvalues for other values of the wall and fluid parameters.

In the present method, we compute the values of the eigenmodes in the examined region where the number of modes can exceed three. The area examined is not necessarily small, and an iterative process

is used only to eliminate the cutoff errors. The eigenvalue search technique developed herein is more efficient and does not produce spurious modes as occasionally encountered when employing the classical QZ search technique used by, for example, Yeo et al.[41,43] to study the absolute instability of a boundary-layer flow over a viscoelastic wall. In contrast to the 6×6 matrix resulting from our search strategy, the QZ search technique results in a matrix size of the order of $4N$, where N is the number of discrete points in the physical space.

To validate our method, it was used to find the least-damped disturbance to Poiseuille flow in a circular, rigid-walled pipe, previously obtained by Gill.[54] The agreement between Gill's results and the present method is excellent, and that agreement is true for both axisymmetric and nonaxisymmetric, temporally damped as well as spatially decaying disturbances. Additionally, the present strategy was used successfully in the case of a noncollapsible compliant tube.[35]

III. Results

We have used the numerical strategy described in Secs. II.F and II.G to study the spatiotemporal stability of the coupled fluid-tube system depicted in Fig. 2 and subjected to infinitesimal axisymmetric or nonaxisymmetric disturbances. The parameters of the system were chosen such that it is stable if the compliant duct is not allowed to collapse; in this way any unstable mode found is expected to be unique to collapsible tubes. Specifically, except for the runs where the tube thickness was varied, we have chosen a thickness of $H - 1 = 0.1$, where Hamadiche and Gad-el-Hak[35] have found that all modes in a similar but noncollapsible tube are stable. We have determined whether a particular instability mode is convective or absolute using the spatiotemporal stability analysis described in Sec. II.E. Searching for cusp points, we have plotted the Laplace contours in the complex frequency plane for all identified modes.

For axisymmetric disturbances corresponding to the azimuthal wave number $n = 0$, we have identified two convective instability modes, one propagating upstream and the other downstream. For each of the nonaxisymmetric disturbances $n = 1, 2, 3, 4, 5, 6$, we have found one absolute instability propagating upstream, whereas for $n = 1, 2$, downstream-propagating convective modes have been observed. In total, we have identified 10 instability modes. All six of the absolute instability modes are replaced by convective modes with the appropriate change of parameters.

We start by showing the effect of changing the tube diameter in the base state and the Reynolds-number effects. Section III.B details the temporal growth rate and frequency of all observed modes and distinguishes between upstream- and downstream-propagating instabilities. This is followed by a closer look at which mode is absolute and which is convective. The following four subsections consider, in turn, the effect of solid viscosity, tube thickness, shear modulus, and finally transmural pressure.

A. Effect of Tube Curvature

Under the action of external pressure, the tube deforms slightly in the base state. In Secs. III.A and II.B, we have shown the effect of transmural pressure on the base diameter and mean flow. We have argued that for sufficiently stiff tubes the tube's radius is a weak function of axial distance. The difference between the present formulation of variable radius and that considering a constant radius in the base state is depicted in Fig. 3. Here we plot the temporal amplification rates s_r and frequency s_i for six upstream-propagating, nonaxisymmetric modes vs the Reynolds number. In all cases, the axial wave number is $k_r = 2$, the shear modulus is $\Gamma = 1$, tube thickness is $H - 1 = 0.1$, solid viscosity is $\mu_r = 0$, external pressure $p_e = 0$, and axial position $X = 4/3$. The temporal amplification rate is plotted in Fig. 3a for the azimuthal wave numbers $n = 1, 2, 3$ and in Fig. 3b for $n = 4, 5, 6$. Similarly, the frequency is plotted in Fig. 3c for $n = 1, 2, 3$ and in Fig. 3d for $n = 4, 5, 6$. In all four parts of the figure, the solid lines indicate the results of the constant diameter formulation, while the broken lines depict the variable diameter results. The difference is small particularly at high Reynolds numbers, consistent with Eq. (7). Beyond a certain value of Reynolds number, higher Reynolds numbers leads to smaller amplification rates, while the frequency of each of the six modes remains approximately constant particularly for $Re > 10^2$. In general, the higher the azimuthal wave number is, the lower the amplification rate and the higher the frequency. The frequency of each successive mode, as n increases from

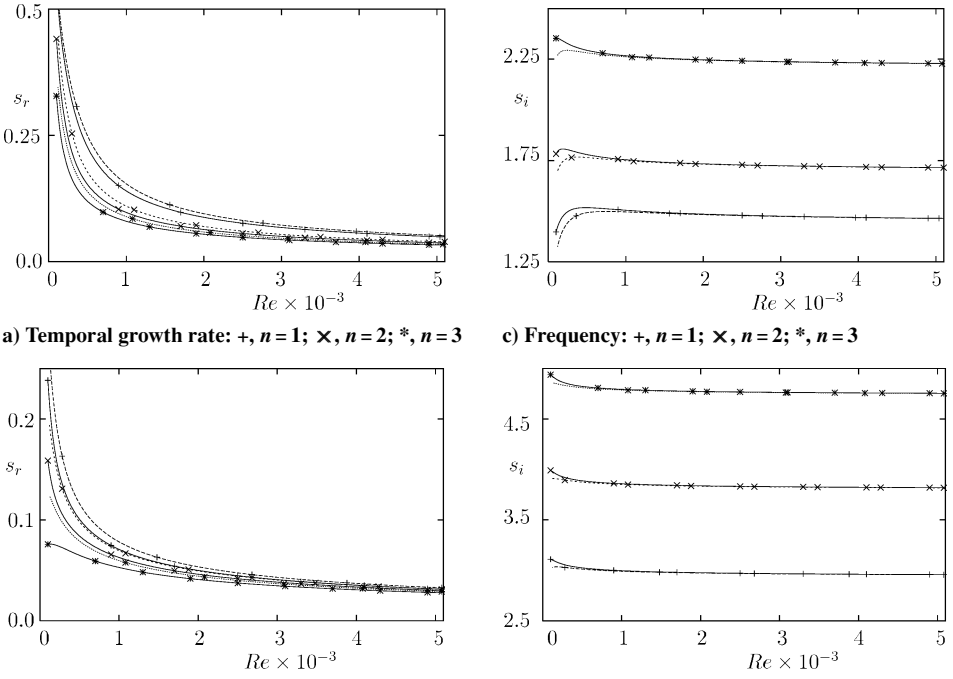

a) Temporal growth rate: +, $n = 1$; ×, $n = 2$; *, $n = 3$

c) Frequency: +, $n = 1$; ×, $n = 2$; *, $n = 3$

b) Temporal growth rate: +, $n = 4$; ×, $n = 5$; *, $n = 6$

d) Frequency: +, $n = 4$; ×, $n = 5$; *, $n = 6$

Fig. 3 Effect of Reynolds number on temporal amplification rate s_r and frequency s_i for six upstream-propagating, nonaxisymmetric modes. Axial wave number $k_r = 2$; shear modulus $\Gamma = 1$; tube thickness $H - 1 = 0.1$; solid viscosity $\mu_r = 0$; external pressure $p_e = 0$; and axial position $X = 4/3$: ——, constant tube diameter in the base state and – – –, variable tube diameter along axial coordinate.

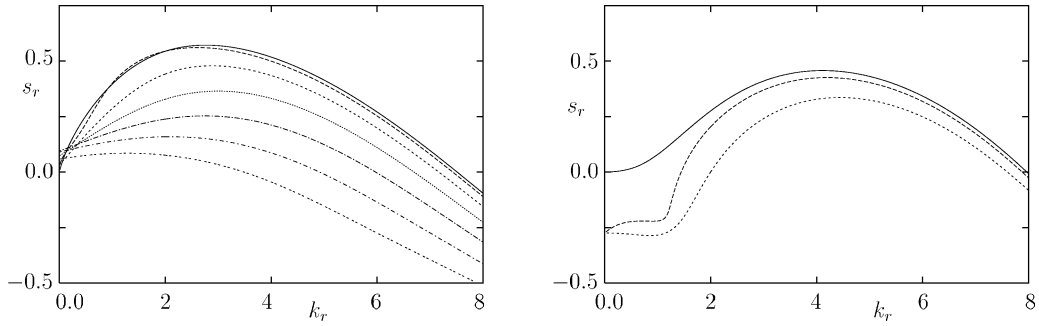

Fig. 4 Temporal growth rate s_r vs axial wavelength k_r for all 10 modes identified herein. Reynolds number $Re = 100$; shear modulus $\Gamma = 1$; tube thickness $H - 1 = 0.1$; and solid viscosity $\mu_r = 0$: a) upstream-propagating waves, azimuthal wave number from top to bottom: $n = 0$; $n = 1$; $n = 2$; $n = 3$; $n = 4$; $n = 5$; and $n = 6$ and b) downstream-propagating waves, azimuthal wave number from top to bottom: $n = 0$; $n = 1$; and $n = 2$.

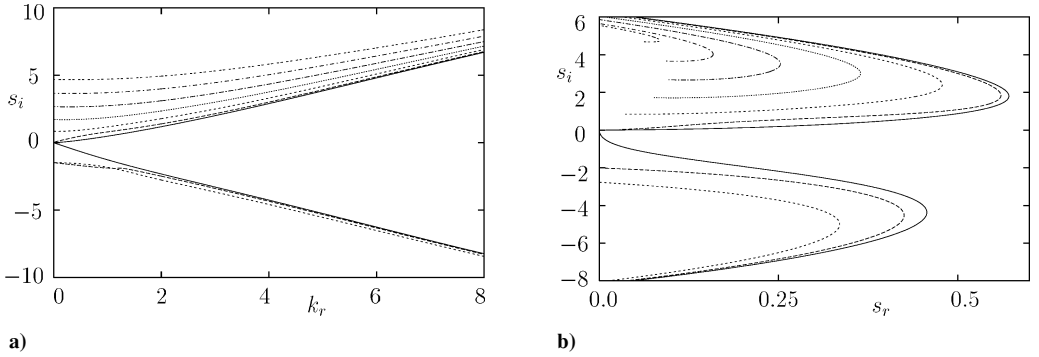

Fig. 5 Unstable frequency s_i for all 10 modes identified herein. Positive frequencies correspond to upstream-propagating modes, and negative frequencies correspond to downstream-propagating modes. Reynolds number $Re = 100$; shear modulus $\Gamma = 1$; tube thickness $H - 1 = 0.1$; solid viscosity $\mu_r = 0$: a) frequency vs axial wave number k_r. For positive frequencies, from bottom, $n = 0$; $n = 1$; $n = 2$; $n = 3$; $n = 4$; $n = 5$; and $n = 6$. For negative frequencies, from top, $n = 0$; $n = 1$; and $n = 2$ and b) frequency vs temporal growth rate s_r. For positive frequencies, from right to left, $n = 0$; $n = 1$; $n = 2$; $n = 3$; $n = 4$; $n = 5$; and $n = 6$. For negative frequencies, from right to left, $n = 0$; $n = 1$; and $n = 2$.

1 to 6, is approximately a constant multiple of the frequency of the first mode.

B. Upstream- and Downstream-Propagating Instabilities

Figure 4 shows the amplification rate vs the axial wave number for all 10 modes identified in this study. The Reynolds number is $Re = 100$, $\Gamma = 1$, $H - 1 = 0.1$, and $\mu_r = 0$. In Fig. 4a, we plot the upstream-propagating modes for the axisymmetric azimuthal wave number $n = 0$ and for the nonaxisymmetric wave numbers $n =$ 1–6. The downstream-propagating modes are plotted in Fig. 4b for $n = 0$ (axisymmetric) and $n = 1, 2$ (nonaxisymmetric). It is clear that the highest growth rates are achieved for modes with smaller azimuthal wave number. Furthermore, the range of axial wave numbers for which the modes are unstable (positive s_r) diminishes as the azimuthal wave number increases. For the same azimuthal wave number, Fig. 4 indicates that the peak amplification rate for the upstream-propagating modes is larger than that for the downstream-propagating ones, and that the peak for the upstream-propagating modes occurs at lower values of the axial wave number k_r. For $n = 0$, the unstable range of axial wave numbers is approximately $k_r = 0$–8, but that range is slightly lower for the upstream-propagating waves at the same azimuthal wave number.

Frequencies corresponding to all of the modes depicted in Fig. 4 are shown in Fig. 5, first against the axial wave number (Fig. 5a) and then against the temporal growth rate (Fig. 5b). Only positive s_r results are plotted. In the figure, the upstream-propagating modes correspond to positive frequencies, and the downstream-propagating modes to negative frequencies. In general, higher azimuthal wave numbers correspond to higher absolute values of frequency but lower growth rates.

The band of unstable frequencies diminishes for higher azimuthal wave numbers, as shown in Fig. 5b. The maximum range of unstable frequencies for the upstream-propagating waves occurs for $n = 0$ and is between 0 and 6. This range is between 0 and -8 for the downstream-propagating waves. Except for small values of k_r, the three downstream-propagating waves have approximately the same negative frequency, which absolute value increases as the axial wavelength increases. The upstream-propagating waves with relatively small amplification rates have the highest positive frequency. Here too, the frequency increases monotonically with k_r.

For $n = 0, 1, 2$, Fig. 5b clearly shows the higher amplification rates for the upstream-propagating waves as compared to those for the downstream-propagating waves. At the azimuthal wave numbers $n = 1, 2$, the system prefers the upstream-propagating modes. As will be shown in Sec. III.C, those nonaxisymmetric modes correspond to absolute instabilities, and the system selects those modes over the nonaxisymmetric convective instabilities.

Figure 5a shows that the slopes of the (s_i, k_r) curves for low values of the axial wave number are very small, indicating correspondingly small group velocities and the possibility that some of those modes might be absolute. We will explore this issue in more detail in the following subsection. In Fig. 5b, the most unstable frequency of the upstream-propagating waves is around 2, and that for the downstream-propagating waves is around -4. For either kind of wave, the most unstable frequencies are shifted toward higher absolute values as the azimuthal wave number increases.

In their experiment with collapsible tubes, Bertram and Godbole[9] observed three distinct modes of oscillations with sharp, discontinuous transitions separating them. They termed the two low-frequency modes *LD* and *LU* and the intermediate-frequency mode *I*. The two low-frequency modes are distinguished by waveform shape: collapse that lasts for approximately half the period for *LD* and brief collapse relative to cycle length for *LU*. The third mode *I* has approximately three times the frequency of the other two and is obtained by transition from the brief-collapse mode as the appropriate parameter is varied. The present results compare most favorably to the experiments of Bertram and Godbole[9] and Bertram and Castles.[10] However, the modes discovered in our analysis are linear

instabilities of a tube in static equilibrium. Of course, the ultimate waveform cannot be predicted by our linear analysis. The experiments dealt with the large-amplitude, often-skewed oscillations of a tube that underwent actual time-dependent collapse. The two situations are different to be sure, but we submit that collapse and nonlinear oscillations can be the climactic manifestation of a linear instability of the coupled fluid-tube system. Nonlinear effects often saturate linear modes; in other words, check the exponential growth of unstable linear modes. Similarities between the linear modes in the present analysis and the experimentally observed nonlinear oscillations support our premise.

In the experiments of Bertram and Godbole,[9] the dimensional frequency f was observed to range from 2.83 to 600 Hz. Their dimensional frequency is related to our dimensionless frequency s_i by the relation

$$f = (1/2\pi)(G/\rho)^{\frac{1}{2}}(s_i/R) \tag{53}$$

Using Bertram and Godbole's values for the duct radius ($R = 0.0065$ m), its density ($\rho = 1000$ kg/m^3), and its circumferential bending stiffness ($K_p = 11{,}400$ N/m^2), their frequency range corresponds to a dimensionless frequency in the range of $s_i = 0.03$–7.26, very close to the range of unstable frequencies predicted by our calculations $s_i = \pm 8$.

C. Absolute and Convective Instabilities

We determined whether a particular instability mode is convective or absolute using the spatiotemporal stability analysis described in Sec. II.E. We plotted the Laplace contours in the complex frequency plane for the 10 instability modes identified in this study, searching for cusp points. An instability mode is considered to be absolute if there is a pinch point in the Fourier contours that prevents the temporal amplification rate from being reduced down to zero even at infinite time. The existence of a pinch point is equivalent to the existence of a saddle point of the dispersion relation in the complex wave-number plane formed by two modes coming from two different halves of that plane. Such a saddle point is equivalent to a cusp point in the complex frequency plane.

To classify an instability mode as absolute or convective, the Laplace contours were carefully examined for some Fourier contours. We focused the search on regions of the parameter space where the group velocity for a particular instability was relatively small. We have found that the Laplace contours corresponding to the upstream-propagated, nonaxisymmetric modes $n = 1$–6 each has a cusp point as clearly seen in Fig. 6, for the conditions $Re = 100$, $\Gamma = 1$, $H - 1 = 0.1$, and $\mu_r = 0$. Therefore, those temporary growing modes (positive s_r) represent absolute instabilities. Under identical conditions, no cusp points with positive temporal amplification rate were found in the Laplace contours for the two axisymmetric

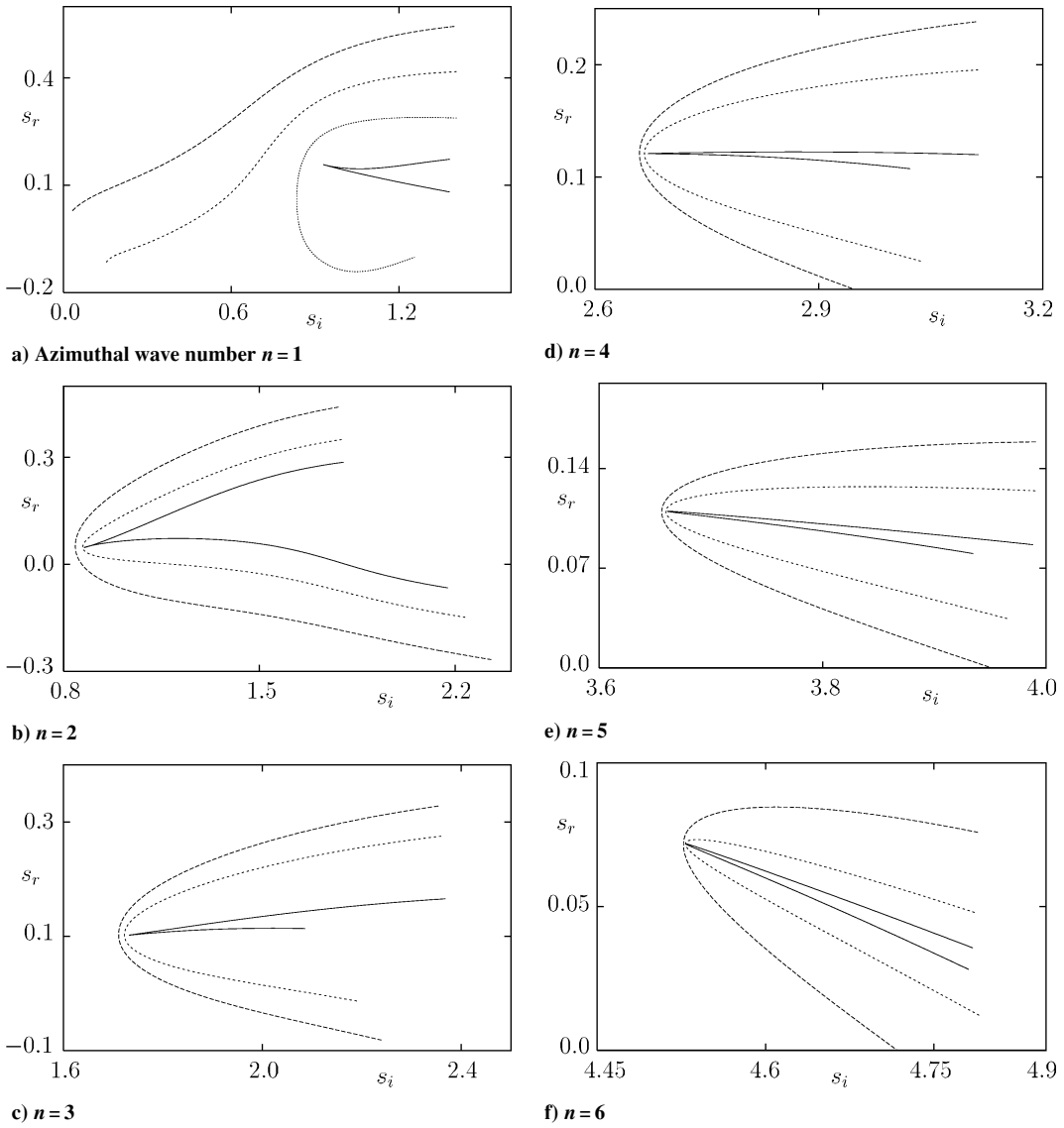

Fig. 6 Laplace contours for six upstream-propagating modes in the vicinity of the cusp points; s_r is the temporal growth rate, and s_i is the frequency. Reynolds number $Re = 100$; shear modulus $\Gamma = 1$; tube thickness $H - 1 = 0.1$; solid viscosity $\mu_r = 0$.

Table 1 Characteristics of the absolute instability modes at their cusp points[a]

Mode	n	k_r	k_i	s_r	s_i
$\boldsymbol{M}_1$	1	0.86	0.72	0.157	0.929
$\boldsymbol{M}_2$	2	0.06	0.24	0.047	0.874
$\boldsymbol{M}_3$	3	0.17	0.28	0.102	1.732
$\boldsymbol{M}_4$	4	0.31	0.25	0.121	2.671
$\boldsymbol{M}_5$	5	0.39	0.19	0.110	3.661
$\boldsymbol{M}_6$	6	0.42	0.13	0.072	4.679

[a] n, azimuthal wave number; k_r, axial wave number; k_i, spatial amplification rate; s_r, temporal amplification rate; and s_i, frequency.

modes identified for $n = 0$ (one propagating upstream and the second downstream) or for the two downstream-propagating, nonaxisymmetric modes $n = 1, 2$. Those four modes are therefore convective instabilities.

According to Kupfer et al.'s theory,[47] the cusp points in each part of Fig. 6 correspond to modes of absolute instabilities that we call mode $\boldsymbol{M}_n$, where the subscript n indicates the azimuthal wave number. The axial wave numbers k_r, spatial amplification rates k_i, temporal amplification rates s_r, and frequencies s_i of the unstable modes $\boldsymbol{M}_1, \ldots, \boldsymbol{M}_6$ at their respective cusp points are summarized in Table 1. These quantities are relevant in that the behavior of the solution for large time is dictated by the frequency and amplification rate at the cusp point.[46]

As can be seen in Table 1, there are two modes, $\boldsymbol{M}_1$ and $\boldsymbol{M}_2$, of approximately equal frequency. These two modes have, respectively, the azimuthal wave numbers $n = 1$ and 2, and so they are different in form, in good agreement with Bertram and Godbole's experimental results.[9] Moreover, the frequency of the unstable mode $\boldsymbol{M}_4$ is three times the frequency of $\boldsymbol{M}_1$ and $\boldsymbol{M}_2$, and that is also in good agreement with the experimental results. The frequency of the other absolutely unstable modes are a multiple of the frequency of $\boldsymbol{M}_1$. For $n = 2$–6, the following relation holds:

$$s_i|_{M_n} \approx (n-1)\, s_i|_{M_1} \tag{54}$$

The obtained frequency ratio in Table 1 is for Reynolds number $Re = 100$, while the experimental results is supposed to be at a much higher, though not precisely known, Reynolds number. Therefore, it is instructive to see if this absolute instability persists at high Reynolds numbers. To do that, one has to solve the following two equations for the temporal amplification rate s_r:

$$D(k, s, Re, \Gamma, H, \mu_r, p_e) = 0 \tag{55}$$

$$\frac{\partial D(k, s, Re, \Gamma, H, \mu_r, p_e)}{\partial k} = 0 \tag{56}$$

A cusp point is a double root of the dispersion relation. An absolute instability therefore is present when the temporal growth rate computed from simultaneously solving Eqs. (55) and (55) is positive. The absolute instability becomes convective when the temporal amplification rate solution of Eqs. (55) and (56) is negative while the amplification rate solution of Eq. (55) alone is positive. Of course if the latter is negative as well, the mode is globally stable.

The zero temporal amplification rate simultaneously satisfying Eqs. (55) and (56) determines the boundary between absolute and convective unstable zone. It is found that the mode $\boldsymbol{M}_1$ becomes convectively unstable at high Reynolds number, whereas the modes $\boldsymbol{M}_2, \ldots, \boldsymbol{M}_6$ remain absolutely unstable at all Reynolds numbers considered here (up to $Re = 5 \times 10^3$).

Figure 7a shows the marginal Reynolds number, based on the temporal amplification rate of the mode $\boldsymbol{M}_1$, vs the wave number. The resulting curve separates the stable and unstable zone, and the unstable region is to the left of that curve. The horizontal line in the figure indicates the boundary between the absolute and convective instability induced by the mode $\boldsymbol{M}_1$. Above a Reynolds number of approximately 200, the absolute instability is replaced by a convective one.

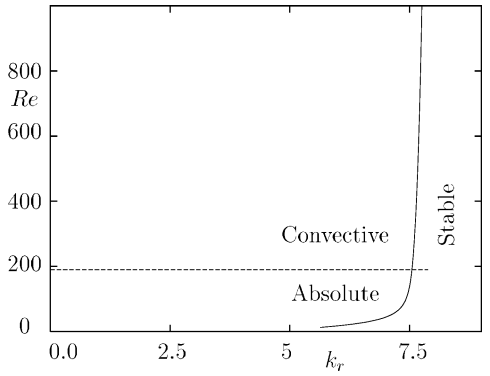

Fig. 7a Marginal stability curve in the plane (Re, k_r) for the absolute mode $\boldsymbol{M}_1$. System is unstable to the left of the ——, and – – – indicates the boundary between absolute and convective instability. The system parameters are shear modulus $\Gamma = 1$; tube thickness $H - 1 = 0.1$; and solid viscosity $\mu_r = 0$.

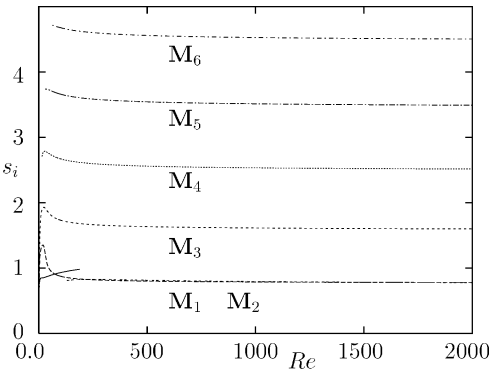

Fig. 7b Frequency of the modes $\boldsymbol{M}_2$–$\boldsymbol{M}_6$, at their respective cusp points, vs Reynolds number. The curve related to the frequency of mode $\boldsymbol{M}_1$ at its cusp point is stopped at $Re \approx 200$ and is replaced by the frequency of its monochromatic, convectively unstable replacement. The system parameters are shear modulus $\Gamma = 1$; tube thickness $H - 1 = 0.1$; and solid viscosity $\mu_r = 0$.

Figure 7b shows the variation of the frequency of the absolute unstable modes at their cusp points as the Reynolds number increases. As can be observed, the frequency ratio of the modes $\boldsymbol{M}_2$ and $\boldsymbol{M}_4$ remains three for all Reynolds numbers. The frequency of the other modes, at their cusp points, is a multiple of the frequency of the mode $\boldsymbol{M}_2$, for all Reynolds numbers. Note that this relation between frequencies exists only at the cusp points. The curve related to the frequency of mode $\boldsymbol{M}_1$ at its cusp point is stopped at $Re \approx 200$ and is replaced by a curve indicating the variation of the frequency of its monochromatic, convectively unstable mode. That frequency is exactly equal to the frequency of mode $\boldsymbol{M}_2$ at its cusp point, for all Reynolds numbers higher than 200.

As mentioned in Sec. III.B, though the modes identified in the present analysis are linear instabilities of a tube in static equilibrium whereas Bertram and Godbole's experiments[9] dealt with the large-amplitude, often-skewed oscillations of a tube that underwent actual time-dependent collapse, nonlinear oscillations can be the climactic manifestation of a linear instability of the coupled fluid-tube system. The analytical results shown in Fig. 7b can be used to explain the experimental results. It is expected in fact that the frequency of the absolutely unstable modes at their cusp points dominates.[46] Therefore, the high-frequency mode observed by Bertram Godbole[9] might be the climactic manifestation of mode $\boldsymbol{M}_4$, and one of their observed low-frequency oscillations can result from mode $\boldsymbol{M}_2$. This is because the ratio between the frequency of these two modes at their respective cusp points is three, as observed in the experiments. Furthermore, if we admit that the frequency is imposed by the absolutely

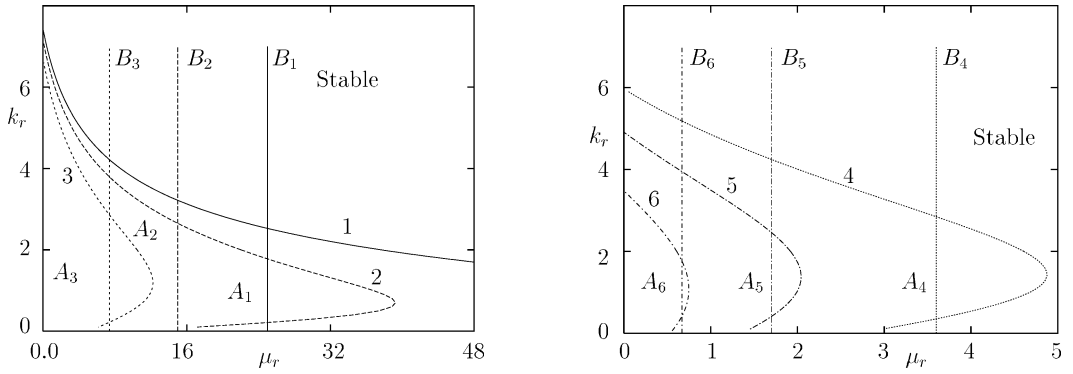

a) Modes M_1; M_2; M_3 **b) Modes M_4; M_5; M_6**

Fig. 8 Marginal stability curves in the (k_r, μ_r) plane. Reynolds number $Re = 100$; shear modulus $\Gamma = 1$; and tube thickness $H - 1 = 0.1$. The number next to each neutral stability curve is the azimuthal wavenumber. The system is unstable to the left of each curve. The vertical lines marked B_n separate the region of absolute and convective instabilities, where the absolute modes are to the left of the vertical lines.

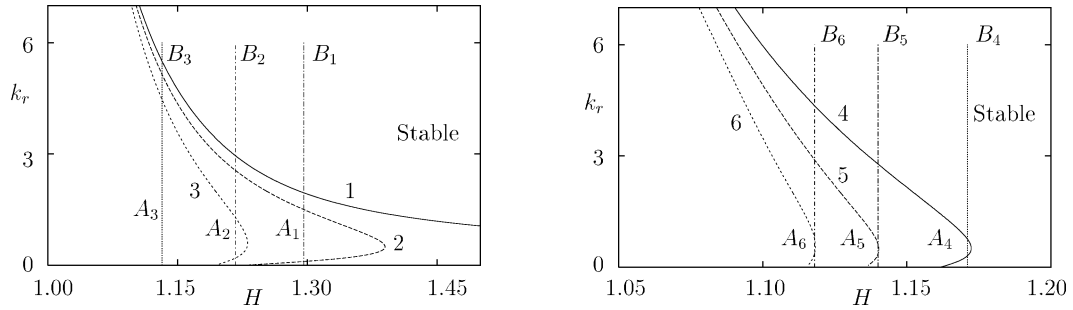

a) Modes M_1; M_2; M_3 **b) Modes M_4; M_5; M_6**

Fig. 9 Marginal stability curves in the (k_r, H) plane. Reynolds number $Re = 100$; shear modulus $\Gamma = 1$; and solid viscosity $\mu_r = 0$. The number next to each neutral stability curve is the azimuthal wave number. The system is unstable to the left of each curve. The vertical lines marked B_n separate the region of absolute and convective instabilities, where the absolute modes are to the left of the vertical lines.

unstable modes, the system has to choose among the convective modes having the same frequency, and this is the monochromatic, convective instability mode that replaces the absolute mode $\boldsymbol{M}_1$. This mode can eventually lead to the other mode of equal frequency but different form observed by Bertram Godbole.[9] The difference in waveform is perhaps because $\boldsymbol{M}_1$ and $\boldsymbol{M}_2$ have different azimuthal wave numbers.

It remains to explain why other modes are not observed in the experiment. Nonlinear selection made by the system in which some unstable modes are simply dampened by nonlinear effects can be a plausible explanation particularly for mode $\boldsymbol{M}_3$. For modes $\boldsymbol{M}_5$ and $\boldsymbol{M}_6$, the temporal growth rates are smaller than those for modes $\boldsymbol{M}_1$–$\boldsymbol{M}_4$, as was shown in Figs. 3 and 5b. Additionally, the solid viscosity strongly dampens those higher frequency modes as will be shown in the following section. Furthermore, a stable equilibrium position in phase space is usually associated with a potential energy minimum. The high-frequency modes, at high azimuthal wave numbers, are associated with high potential energy storage in the solid medium and can therefore constitute unstable dynamic equilibrium positions, hence unobservable.

D. Effect of Solid Viscosity

We investigated the effect of solid viscosity on the six absolute instability modes identified in this study. The solid viscosity ranged from 0 (elastic solid) to 50 times that of the fluid. We determined the stability boundary as well as identified the conditions under which an absolute instability is replaced by a convective one.

Figure 8 shows the marginal stability curves in the (k_r, μ_r) plane, where k_r is the axial wave number and μ_r is the ratio of solid to fluid viscosity. Modes $\boldsymbol{M}_1$, $\boldsymbol{M}_2$, and $\boldsymbol{M}_3$ are depicted in Fig. 8a, while modes $\boldsymbol{M}_4$, $\boldsymbol{M}_5$, and $\boldsymbol{M}_6$ are shown in Fig. 8b. The neutral curve corresponding to mode $\boldsymbol{M}_1$ is truncated for scale commodity. For each mode, the unstable zone is to the left of the neutral stability curve. The vertical lines B_n mark the boundaries between absolute and convective instabilities, where the absolute instability is to the left of each of the respective vertical lines and is marked A_1, A_2, etc. The problem parameters for all cases are Reynolds number $Re = 100$, shear modulus $\Gamma = 1$, and thickness $H - 1 = 0.1$. Solid viscosity clearly dampens all of the unstable modes, but the effect is stronger for high-azimuthal-wave-number (i.e., high-frequency) modes. In other words, a viscoelastic solid is susceptible to only small-azimuthal-wave-number instabilities. This might explain the absence of instabilities corresponding to modes $\boldsymbol{M}_5$ and $\boldsymbol{M}_6$ in Bertram and Godbole's experiments.[9] Increasing the solid viscosity causes the absolute instability modes to be replaced by convective ones. This transformation takes place at modest solid viscosities for the high-azimuthal-waven-umber modes.

E. Effect of Wall Thickness

The effect of wall thickness $[H - 1]$ on the six absolute instability modes identified in this research was investigated. The tube thickness ranged from 0 to 50% of its radius. We determined the stability boundary as well as identified the conditions under which an absolute instability is replaced by a convective one.

Figure 9 shows the marginal stability curves in the (k_r, H) plane, where k_r is the axial wave number and $[H - 1]$ is the ratio of the tube thickness to its local radius. Modes $\boldsymbol{M}_1$, $\boldsymbol{M}_2$, and $\boldsymbol{M}_3$ are depicted in Fig. 9a, while modes $\boldsymbol{M}_4$, $\boldsymbol{M}_5$, and $\boldsymbol{M}_6$ are shown in Fig. 9b. The neutral curve corresponding to the mode $\boldsymbol{M}_1$ is truncated for scale commodity. For each mode, the unstable zone is to the left of the neutral stability curve. The vertical lines B_n mark the boundaries between absolute and convective instabilities, where the absolute instability is to the left of each of the respective vertical lines, and is marked A_1, A_2, etc. The problem parameters for all cases are Reynolds number $Re = 100$, shear modulus $\Gamma = 1$, and solid viscosity $\mu_r = 0$.

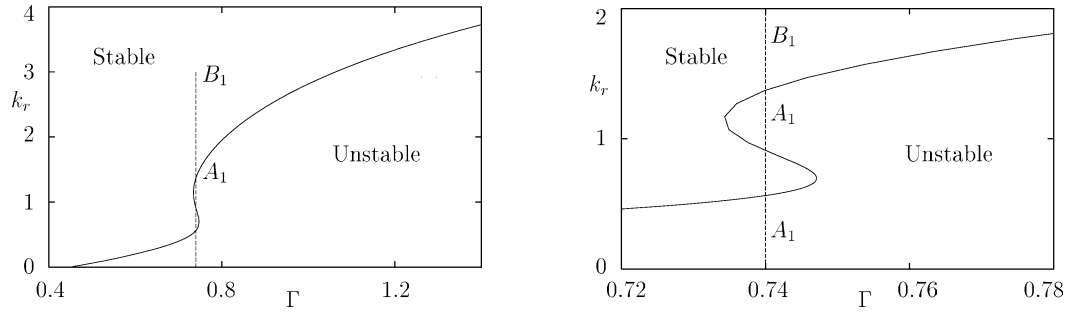

Fig. 10 Marginal stability curve of mode M_1 in the (k_r, Γ) plane. Reynolds number $Re = 100$; tube thickness $H - 1 = 0.1$; and solid viscosity $\mu_r = 0$. The unstable zone is to the right of the curve. The vertical line marked B_1 separates the region of absolute and convective instability, where the absolute mode is to the right of that lines. Panel b is a zoomed-in version of panel a.

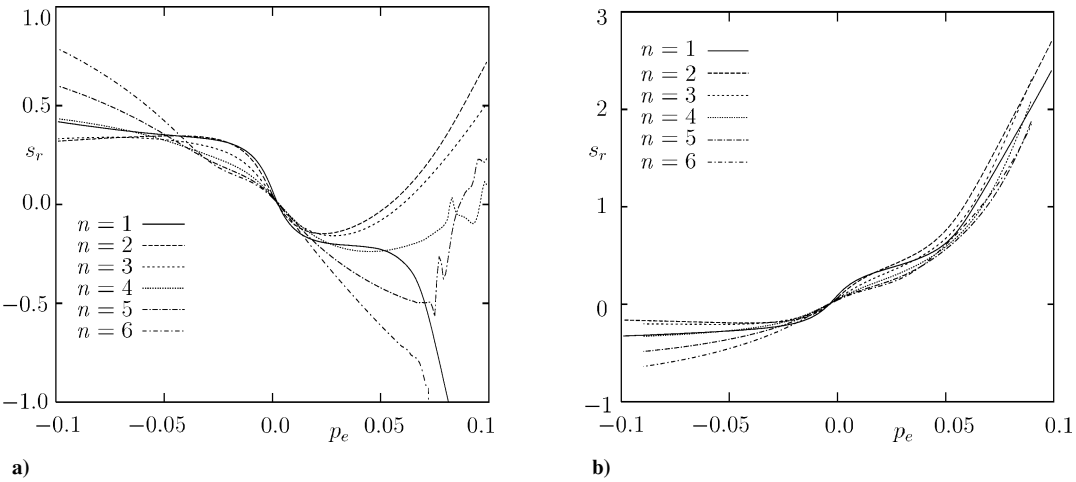

Fig. 11 Temporal growth rate s_r vs external pressure p_e for all six absolute instability modes. Axial wave number $k_r = 2$; Reynolds number $Re = 2100$; thickness $H - 1 = 0.1$; shear modulus $\Gamma = 1$; and solid viscosity $\mu_r = 0$: a) axial position $X = 2/3$ and b) $X = 4/3$. The legends in the inserts indicate the values of the azimuthal wave number n.

Increasing the thickness of the tube stabilizes all modes, but the effect is stronger for the high-azimuthal-wave-number (i.e., high-frequency) modes. Increasing the tube thickness causes the absolute instability modes to be replaced by convective ones. Again, this effect is stronger for the high-azimuthal-wave-number modes. For modes $\boldsymbol{M}_5$ and $\boldsymbol{M}_6$, the absolute oscillations are stabilized prior to being replaced by convective instabilities. In other words, those two instability modes remain absolute regardless of the tube thickness. But other than that, increasing the tube thickness has an analogous effect on the different absolute instability modes as increasing the viscosity of the solid. A thin, viscoelastic tube behaves similarly to a thick, elastic one.

F. Effect of Shear Modulus

The effect of the wall compliance on the six absolute instability modes identified in this research was investigated. The dimensionless compliance ranged from 0.4 (stiff tube) to 1.6 (soft tube). We determined the stabilty boundary as well as identified the conditions under which an absolute instability is replaced by a convective one.

Figure 10 shows the marginal stability curve for mode $\boldsymbol{M}_1$ in the (k_r, Γ) plane, where k_r is the axial wave number and Γ^2 is the ratio of the dynamic pressure, based on the local velocity maximum and the solid's shear modulus. Figure 10b is a zoomed-in version of Fig. 10a. The problem parameters are Reynolds number $Re = 100$, thickness $H - 1 = 0.1$, and solid viscosity $\mu_r = 0$. The unstable zone is to the right of the neutral stability curve (softer material). The vertical line B_1 marks the boundary between absolute and convective instability, where the absolute instability is to the right of the line and is marked A_1. Stiffer tubes are, as expected, more stable. An absolute instability is replaced by a convective one as the tube stiffens, but that new instability is ultimately stabilized as the tube stiffens further. Figure 10b indicates that there a multiplicity of the critical wave number for certain values of Γ near the boundary of absolute and convective instabilities.

Increasing the shear modulus of the viscoelastic material (i.e., decreasing Γ) stabilizes all of the other absolute modes ($\boldsymbol{M}_2$–$\boldsymbol{M}_6$) to different degrees, but without passing by a convective instability first as is the case for mode $\boldsymbol{M}_1$. The tube's shear modulus, thickness, and viscosity all have an analogous effect in that they are all stabilizing.

G. Effect of Transmural Pressure

We investigated the effect of transmural pressure on the six absolute instability modes identified herein. The dimensionless external pressure $([p_e - p_u]/G)$ ranged from -0.1 to $+0.1$. A negative transmural pressure (i.e., zero or positive dimensionless p_e) leads to a convergent–divergent tube in the base state, whereas a positive transmural pressure leads to a divergent–convergent tube. This effect was quantified in Sec. III.A. The problem parameters for the cases investigated in this section are tube length of $L = 2$ (in units of inlet radius), axial wave number $k_r = 2$, Reynolds number $Re = 2.1 \times 10^2$, thickness $H - 1 = 0.1$, shear modulus $\Gamma = 1$, and solid viscosity $\mu_r = 0$. For each mode, we computed the temporal growth rate s_r at each downstream location in the range of $X = 0$–2.

Figures 11a and 11b depict the temporal growth rate vs external pressure for, respectively, the two downstream stations $X = 2/3$ and 4/3. In the upstream part of the tube (Fig. 11a), the absolute modes grow when p_e is negative (positive transmural pressure). Conversely, at $X = 4/3$ (Fig. 11b) the absolute modes grow when p_e is positive (negative transmural pressure).

In Figs. 12a and 12b, we plot s_r vs the axial location X for, respectively, $p_e = 0.03$ and $p_e = -0.03$. The form of the channel in the base state is indicated in each figure by the function $\delta(X)$. The

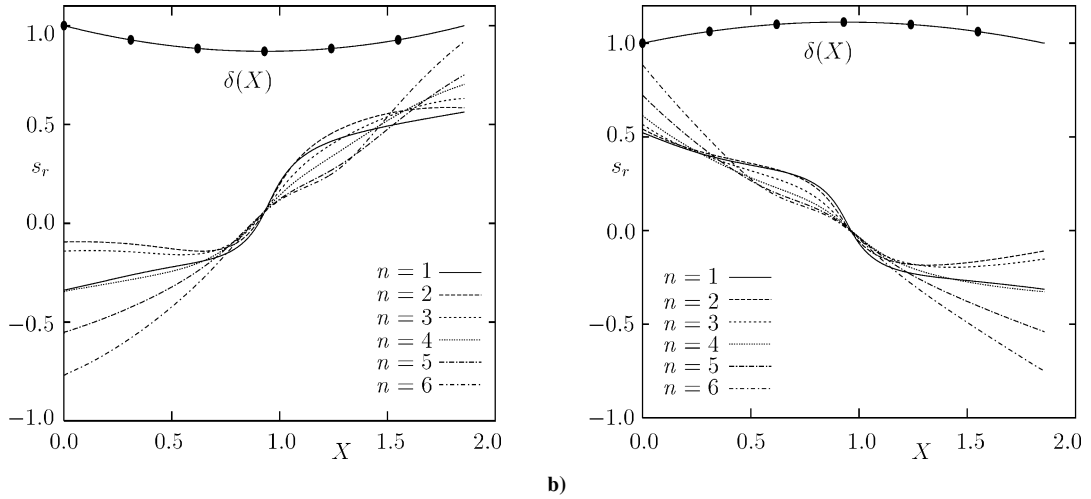

Fig. 12 Temporal growth rate s_r vs axial position X for all six absolute instability modes. Axial wave number $k_r = 2$; Reynolds number $Re = 2100$; thickness $H-1 = 0.1$; shear modulus $\Gamma = 1$; and solid viscosity $\mu_r = 0$. The solid circles and the curve labeled $\delta(X)$ mark the form of the tube in the base state: a) external pressure $p_e = 0.03$ and b) $p_e = -0.03$. The legends in the inserts indicate the values of the azimuthal wave number n.

tube takes a convergent–divergent form in the first figure where the transmural pressure is negative, and a divergent–convergent form in the second figure where the transmural pressure is positive. It is clear that the growth of the absolute modes is always associated with the divergent portion of the tube, be it the downstream portion of the tube for negative transmural pressure or the upstream portion of the tube for positive transmural pressure. It seems likely that the favorable pressure gradient in the convergent portion of the duct has a stabilizing influence on the standing waves.

IV. Conclusions

Fluid conduits that are capable of collapse are commonly found in nature as well as in man-made systems. A tube typically buckles nonaxisymmetrically, and, under steady supply conditions, the throat area might reach a new lower asymptote or might oscillate periodically or even chaotically. Understanding this complex dynamics is important and will enable the designer of soft tubes to prevent, control, or exploit the collapse phenomenon.

In the present research, we advanced the view that collapse and oscillations can be the climactic manifestation of an instability of the coupled fluid-tube system. We therefore studied the linear stability of the system prior to the onset of dynamic collapse. The stability of the Hagen–Poiseuille flow of a Newtonian fluid in an incompressible, collapsible, viscoelastic tube was determined using linear stability analysis. A novel numerical strategy was introduced to study the spatiotemporal stability of the coupled fluid-structure system subjected to infinitesimal axisymmetric or nonaxisymmetric disturbances. The strategy alleviated the need for an initial guess and thus ensured that all of the unstable modes within a given closed region in the complex eigenvalue plane would be found. The stiff nature of the governing equations dictated the use of the method of orthonormalization in order to achieve rapid convergence. The dimensionless parameters investigated were the external pressure, the Reynolds number, and the tube's stiffness, its thickness, and its viscosity. The parameters of the system were chosen such that it is stable if the compliant duct is not allowed to collapse, in this way any unstable mode found is expected to be unique to collapsible tubes.

As a base state, we assumed a finite-length flexible tube anchored at both ends and surrounded by a large pressurized chamber of constant pressure. As a result of a pressure-driven base flow inside, the tube is subjected, along its length, to an increasingly negative transmural pressure. Consequently, the flexible tube deforms slightly into a convergent–divergent geometry (or a divergent–convergent one in case of a positive transmural pressure). For sufficiently stiff tubes, the base geometry is axisymmetric, and the tube diameter is a weak function of the axial coordinate. We explicitly computed this function using the steady equation of linear elasticity. However, the base flow inside the convergent–divergent channel was assumed, to first order, to be locally parallel and parabolic. This approach clearly excludes the complex flow associated with the geometry of a noncircular, convergent–divergent nozzle and the oscillations caused by the choking phenomenon, but allowed us to investigate a first-principles, arbitrary-Reynolds-number system considerably more general and less ad hoc than that afforded by the lumped-parameter, the one-two-dimensional, or the zero-Reynolds-number models. Similarities between the linear modes in the present analysis and the experimentally observed nonlinear oscillations supported our premise.

For axisymmetric disturbances corresponding to the azimuthal wave number $n = 0$, we have identified two convective instability modes, one propagating upstream and the other downstream. For each of the nonaxisymmetric disturbances $n = 1, 2, 3, 4, 5, 6$, we have found one absolute instability propagating upstream, whereas for $n = 1, 2$ downstream-propagating convective modes have been observed. In total, we have identified 10 instability modes. All six of the absolute instability modes are replaced by convective modes with the appropriate change of parameters.

Two of the standing waves have equal frequencies at their respective cusp points, whereas a third absolute instability has triple that frequency, in excellent agreement with existing experiments. This frequency tripling is preserved for all Reynolds numbers. The $n = 1$ absolute instability mode is replaced by a convective mode when the Reynolds number exceeds 200, whereas the other standing waves, at $n = 2$–6, persist to high-Reynolds-number values. Increasing the solid's viscosity, thickness, or shear modulus causes the absolute instability modes to become convective as well as to ultimately become stable. Those effects are stronger for the high-azimuthal-wave-number modes. The boundaries separating the zone of absolute instabilities from that of convective instabilities have been identified.

A negative transmural pressure leads to a convergent–divergent tube in the base state, whereas a positive transmural pressure leads to a divergent–convergent tube. The growth of the absolute modes is always associated with the divergent portion of the tube, be it the downstream portion of the tube for negative transmural pressure or the upstream portion of the tube for positive transmural pressure. It seems likely that the favorable pressure gradient in the convergent portion of the duct has a stabilizing influence on the standing waves.

While maintaining the locally parallel-flow assumption, the present linear stability analysis should be extended to nonlinear one. Conditions under which the nonlinear dynamical system becomes chaotic will be of great practical interest. Finally, nonaxisymmetric, strongly variable-diameter tubes are much more complex to analyze as compared to the present axisymmetric, weakly variable-diameter tubes, but such analysis will be a very worthwhile endeavor.

Experimentally, tube collapse is invariably nonaxisymmetric, whereas tube blowup is typically axisymmetric. Perhaps one can start with a steady base flow in a strongly convergent–divergent tube and relax the locally parallel-flow assumption invoked in the present investigation. Linear stability analysis of this base flow can then be conducted to find the resulting instability modes and compare these to the modes identified in the present study. The model complexity can be gradually increased to ultimately solve a realistic collapsible tube problem using only first principles.

References

[1]Kamm, R. D., and Pedley, T. J., "Flow in Collapsible Tubes: A Brief Review," *Journal of Biomechanical Engineering*, Vol. 111, 1989, pp. 177–179.

[2]Conrad, W. A., "Pressure–Flow Relationships in Collapsible Tubes," *IEEE Transactions on Bio-Medical Engineering*, Vol. 16, No. 4, 1969, pp. 284–295.

[3]Griffiths, D. J., "Oscillations in the Outflow from a Collapsible Tube," *Medical and Biological Engineering and Computing*, Vol. 15, No. 4, 1977, pp. 357–362.

[4]Bertram, C. D., Raymond, C. J., and Pedley, T. J., "Mapping of Instabilities for Flow Through Collapsed Tubes of Differing Length," *Journal of Fluids and Structures*, Vol. 4, No. 2, 1990, pp. 125–153.

[5]Bertram, C. D., Raymond, C. J., and Pedley, T. J., "Application of Nonlinear Dynamics Concepts to the Analysis of Self-Excited Oscillations of a Collapsible Tube Conveying a Fluid," *Journal of Fluids and Structures*, Vol. 5, No. 4, 1991, pp. 391–426.

[6]Bertram, C. D., "Two Modes of Instability in a Thick-Walled Collapsible Tube Conveying a Flow," *Journal of Biomechanics*, Vol. 15, No. 3, 1982, pp. 223–224.

[7]Elad, D., Sahar, M., Avidor, J. M., and Einav, S., "Steady Flow Through Collapsible Tubes: Measurements of Flow and Geometry," *Journal of Biomechanical Engineering*, Vol. 114, No. 1, 1992, pp. 84–91.

[8]Bertram, C. D., Sheppeard, M. D., and Jensen, O. E., "Prediction and Measurement of the Area–Distance Profile of Collapsed Tubes During Self-Excited Oscillation," *Journal of Fluids and Structures*, Vol. 8, No. 6, 1994, pp. 637–660.

[9]Bertram, C. D., and Godbole, S. A., "Area and Pressure Profiles for Collapsible-Tube Oscillations of Three Types," *Journal of Fluids and Structures*, Vol. 9, No. 3, 1995, pp. 257–277.

[10]Bertram, C. D., and Castles, R. J., "Flow Limitation in Uniform Thick-Walled Collapsible Tubes," *Journal of Fluids and Structures*, Vol. 13, No. 3, 1999, pp. 399–418.

[11]Kounanis, K., and Mathioulakis, D. S., "Experimental Flow Study Within a Self-Oscillating Collapsible Tube," *Journal of Fluids and Structures*, Vol. 13, No. 1, 1999, pp. 61–73.

[12]Shapiro, A. H., "Steady Flow in Collapsible Tubes," *Journal of Biomechanical Engineering*, Vol. 99, Aug. 1977, pp. 126–147.

[13]Kamm, R. D., and Shapiro, A. H., "Unsteady Flow in a Collapsible Tube Subjected to External Pressure or Body Forces," *Journal of Fluid Mechanics*, Vol. 95, Nov. 1979, pp. 1–78.

[14]Bertram, C. D., and Pedley, T. J., "A Mathematical Model of Unsteady Collapsible Tube Behaviour," *Journal of Biomechanics*, Vol. 15, No. 1, 1982, pp. 39–50.

[15]Cancelli, C., and Pedley, T. J., "A Separated-Flow Model for Collapsible-Tube Oscillations," *Journal of Fluid Mechanics*, Vol. 157, Aug. 1985, pp. 375–404.

[16]Jensen, O. E., and Pedley, T. J., "The Existence of Steady Flow in a Collapsed Tube," *Journal of Fluid Mechanics*, Vol. 206, Sept. 1989, pp. 339–374.

[17]Jensen, O. E., "Instabilities of Flow in a Collapsed Tube," *Journal of Fluid Mechanics*, Vol. 220, Nov. 1990, pp. 623–659.

[18]Jensen, O. E., "Chaotic Oscillations in a Simple Collapsible-Tube Model," *Journal of Biomechanical Engineering*, Vol. 114, No. 1, 1992, pp. 55–59.

[19]Pedley, T. J., "Longitudinal Tension Variation in Collapsible Cchannels: a New Mechanism for the Breakdown of Steady Flow," *Journal of Biomechanical Engineering*, Vol. 114, No. 1, 1992, pp. 60–67.

[20]Heil, M., "Stokes Flow in Collapsible Tubes: Computation and Experiment," *Journal of Fluid Mechanics*, Vol. 353, Dec. 1997, pp. 285–312.

[21]Pedrizzetti, G., "Fluid Flow in a Tube with an Elastic Membrane Insertion," *Journal of Fluid Mechanics*, Vol. 375, Nov. 1998, pp. 39–64.

[22]Hayshi, S., Hayase, T., and Kawamura, H., "Numerical Analysis for Stability and Self-Exited Oscillation in Collapsible Tube Flow," *Journal of Biomechanical Engineering*, Vol. 120, No. 4, 1998, pp. 468–475.

[23]Luo, X. Y., and Pedley, T. J., "Multiple Solutions and Flow Limitation in Collapsible Channel Flows," *Journal of Fluid Mechanics*, Vol. 420, Oct. 2000, pp. 301–324.

[24]Pedley, T. J., "Blood Flow in Arteries and Veins," *Perspectives in Fluid Dynamics: A Collective Introduction to Current Research*, edited by G. K. Batchelor, H. K. Moffatt, and M. G. Worster, Cambridge Univ. Press, London, 2000, pp. 105–158.

[25]Carpenter, P. W., and Pedley, T. J. (eds)., *Flow past Highly Compliant Boundaries and in Collapsible Tubes*, Kluwer, Dordrecht, The Netherlands, 2003.

[26]Moreno, A. H., Katz, A. I., Gold, L. D., and Reddy, R. V., "Mechanics of Distension of Dog Veins and Other Very Thin-Walled Tubular Structures," *Circulation Research*, Vol. 27, No. 6, 1970, pp. 1069–1081.

[27]Abdel-Aziz, Y. I., and Karara, H. M., "Direct Linear Transformation from Comparator Coordinates into Object Space Coordinates in Close-Range Photogrammetry," *Close-Range Photogrammetry, Proceedings of the ASP/UI Symposium*, American Society of Photogrammetry, Falls Church, VA, 1971, pp. 1–18.

[28]Lambert, R. K., Pack, R. J., Xia, Y., Eccles, C. D., and Callaghan, P. T., "In Vitro Tracheal Mechanics by Nuclear Magnetic Resonance," *Journal of Applied Physiology*, Vol. 65, No. 2, 1988, pp. 1872–1879.

[29]Bertram, C. D., and Ribreau, C., "Cross-Sectional Area Measurement in Collapsible Tubes Using the Transformer Principle," *Medical and Biological Engineering and Computing*, Vol. 27, No. 4, 1989, pp. 357–364.

[30]Thiriet, M. Z., Maarek, J. M., Chartrand, D. A., Delpuech, C., Davis, L., Hatzfeld, C., and Chang, H. K., "Transverse Images of the Human Thoracic Trachea during Forced Expiration," *Journal of Applied Physiology*, Vol. 67, No. 3, 1989, pp. 1032–1040.

[31]McClurken, M. E., "Shape-Independent Area Measurement in Collapsible Tubes by an Electrical Impedance Technique," *Proceedings of the Thirty-First Annual Conference on Engineering in Medicine and Biology*, 1978, p. 95.

[32]Bertram, C. D., "The Effect of Wall Thickness, Axial Strain and End Proximity on the Pressure–Area Relation of Collapsible Tubes," *Journal of Biomechanics*, Vol. 20, No. 9, 1987, pp. 863–876.

[33]Schaldach, M., "Automatic Adjustment of Pacing Parameters Based on Intracardiac Impedance Measurements," *Pacing and Clinical Electrophysiology*, Vol. 13, No. 12, Pt. 2, 1990, pp. 1702–1710.

[34]Grotberg, J. B., and Gavriely, N., "Flutter in Collapsible Tubes: A Theoretical Model of Wheezes, *Journal of Applied Physiology*, Vol. 66, 1989, pp. 2262–2273.

[35]Hamadiche, M., and Gad-el-Hak, M., "Temporal Stability of Flow Through Viscoelastic Tubes," *Journal of Fluids and Structures*, Vol. 16, No. 3, 2002, pp. 331–359.

[36]Evrensel, C. A., Khan, M. R., Elli, S., and Krumpe, P. E., "Viscous Airflow through a Rigid Tube with a Compliant Lining: A Simple Model for the Air–Mucus Interaction in Pulmonary Airways," *Journal of Biomechanical Engineering*, Vol. 115, No. 3, 1993, pp. 262–270.

[37]Kumaran, V., "Stability of Wall Modes in a Flexible Tube," *Journal of Fluid Mechanics*, Vol. 362, May 1998, pp. 1–15.

[38]Landau, L. D., and Lifshitz, E. M., *Theory of Elasticity*, 2nd ed., Pergamon, Oxford, 1970 (translated from the Russian).

[39]Brazier-Smith, P. R., and Scott, J. F., "Stability of Fluid Flow in the Presence of a Compliant Surface," *Wave Motion*, Vol. 6, No. 6, 1984, pp. 547–560.

[40]Huerre, P., and Monkewitz, P. A., "Local and Global Instabilities in Spatially Developing Flows," *Annual Review of Fluid Mechanics*, Vol. 22, Jan. 1990, pp. 473–537.

[41]Yeo, K. S., Khoo, B. C., and Zhao, H. Z., "The Absolute Instability of Boundary-Layer Flow over Viscoelastic Walls," *Theoretical and Computational Fluid Dynamics*, Vol. 8, No. 4, 1996, pp. 237–252.

[42]Lingwood, R. J., "On the Application of the Briggs' and Steepest-Descent Methods to a Boundary-Layer Flow," *Studies in Applied Mathematics*, Vol. 98, No. 3, 1997, pp. 213–254.

[43]Yeo, K. S., Khoo, B. C., and Zhao, H. Z., "The Convective and Absolute Instability of Fluid Flow over Viscoelastic Compliant Layers," *Journal of Sound and Vibration*, Vol. 223, No. 3, 1999, pp. 379–398.

[44]Huerre, P., "Open Shear Flow Instabilities," *Perspectives in Fluid Dynamics: A Collective Introduction to Current Research*, edited by G. K. Batchelor, H. K. Moffatt, and M. G. Worster, Cambridge Univ. Press, London, 2000, pp. 159–229.

[45]Yeo, K. S., Zhao, H. Z., and Khoo, B. C., "Turbulent Boundary Layer over a Compliant Surface: Absolute and Cconvective Instabilities," *Journal of Fluid Mechanics*, Vol. 449, Dec. 2001, pp. 141–168.

[46]Briggs, R. J., *Electron-Stream Interaction with Plasmas*, MIT Press, Cambridge, MA, 1964.

[47]Kupfer, K., Bers, A., and Ram, A. K., "The Cusp Map in the Complex-Frequency Plane for Absolute Instabilities," *Physics of Fluids*, Vol. 30, No. 10, 1987, pp. 3075–3082.

[48]Doaré, O., and de Langre, E., "Local and Global Instabilities of Fluid-Conveying Pipes on Elastic Foundation," *Journal of Fluids and Structures*, Vol. 16, No. 1, 2002, pp. 1–14.
[49]Scott, M. R., and Watts, H. A., "Computational Solution of Linear Two-Point Boundary Value Problems via Orthonormalization," *SIAM Journal of Numerical Analysis*, Vol. 14, No. 1, 1977, pp. 40–70.
[50]Garg, V. K., and Rouleau, W. T., "Linear Spatial Stability of Pipe Poiseuille Flow," *Journal of Fluid Mechanics*, Vol. 54, July 1972, pp. 113–127.
[51]Hamadiche, M., "Instabilité de l'Écoulement de Poiseuille en Conduite Viscoélastique Cylindrique," *3eme Congrès de Mécanique*, Faculté des Sciences de Tétouan, April 1997.
[52]Hamadiche, M., "Instabilité Causée par l'Interaction Fluide/Structure," *34eme Colloque d'Aérodynamique Appliqué de la A.A.A.F.*, March 1998.
[53]Lelong-Ferrand, J., and Arnaudiès, J. M., *Cours de Mathématiques, Algèbre, Tome 1*, Dunod Univ., Bordas, Paris, 1977.
[54]Gill, A. E., "The Least-Damped Disturbance to Poiseuille Flow in a Circular Pipe," *Journal of Fluid Mechanics*, Vol. 61, Oct. 1973, pp. 97–107.

S. Mahalingam
Associate Editor